
# Elastic wave scattering in metamaterials with localized defects

Charles Dorn

PII: S0022-460X(26)00028-3
DOI: https://doi.org/10.1016/j.jsv.2026.119663
Reference: YJSVI 119663

To appear in: *Journal of Sound and Vibration*

Received date: 28 July 2025
Revised date: 24 November 2025
Accepted date: 12 January 2026

Please cite this article as: Charles Dorn, Elastic wave scattering in metamaterials with localized defects, *Journal of Sound and Vibration* (2025), doi: https://doi.org/10.1016/j.jsv.2026.119663

**Highlights**

- Semi-analytical modeling is developed for waves in metamaterials with defects
- Applies to metamaterials with dispersion relations only available numerically
- Computational efficiency of our model enables its use in inverse problems
- Inverse design of defects in a metamaterial is demonstrated for wave guiding

# Elastic wave scattering in metamaterials with localized defects

Charles Dorn[1]

[1]*Department of Aeronautics & Astronautics, University of Washington, Seattle, USA, cdorn@uw.edu*

**Abstract**

This work presents a semi-analytical multiple scattering formulation for elastic waves in periodic media with defects. We model the scattering of Bloch waves interacting with defects of arbitrary styrength that are on a length scale much smaller than relevant wavelengths. The basis for the proposed framework is the far-field asymptotic approximation of the lattice Green's function represented in terms of Bloch eigenfunctions. Thus, it is applicable to any periodic material whose dispersion relations and corresponding mode shapes are available either analytically or numerically. The local perturbation method is used to resolve the singularity in the far-field lattice Green's function, enabling the derivation of a tractable multiple scattering system. Examples are presented showing agreement between the scattering model and high-fidelity transient simulations in the context of a mass-spring network and a beam-based metamaterial. The proposed modeling framework is computationally efficient, opening the door to inverse problems such as the design of defects for wave manipulation. We present the inverse design of a set of defects embedded in a periodic metamaterial for wave guiding, demonstrating that our scattering model is an effective tool for exploring the vast design space of defect engineering in metamaterials.

*Keywords*: metamaterial, multiple scattering, Bloch wave, lattice Green's function, elasticity, inverse design

## 1. Introduction

Metamaterials exhibit microstructures that are engineered to achieve effective properties out of reach of natural materials. While idealized periodic architectures are often studied, understanding the role of defects is crucial for the application of metamaterials. On the one hand, the inevitable presence of manufacturing defects and damage has a strong impact on the actual effective properties of metamaterials [1]. On the other hand, purposeful introduction of defects offers an opportunity to expand the metamaterial design space, promising novel functionalities. Thus, the modeling of defects is critical for both characterization and design of metamaterial architectures. This work presents a semi-analytical modeling framework that captures elastic wave scattering in lattices with defects, providing a computationally efficient tool for simulating defective metamaterials.

Efficient modeling is the foundation for effective characterization and design of metamaterials. However, the multiscale nature of metamaterials introduces a computational bottleneck. While perfectly periodic architectures benefit from Bloch's theorem that enables a single unit cell to be representative of an entire lattice [2], any deviation from periodicity (e.g., due to defects) significantly complicates computations. High-fidelity simulations, for example, based on transient finite element (FE) analysis, are reliable but inefficient due to the short length and time scales that must be resolved. Therefore, approximations that lead to efficient modeling are crucial, especially when pursuing inverse problems that require repeated evaluation of a forward model. To this end, we develop efficient semi-analytical modeling of elastic wave scattering due to defects in a lattice.

The study of defects in lattices has a rich history, tracing back to the theoretical models of defective atomic lattices in [3, 4, 5, 6, 7] among others. Defective lattice dynamics is typically studied from two perspectives. The first is near the defect, where localized modes in the neighborhood of the defect can support frequencies otherwise forbidden by the perfect lattice (i.e., within the bandgaps of the perfect lattice). The second regime captures the far-field dynamics away from the defect, concerning the scattering of an incident wave due to a defect (i.e., within the pass-bands of the perfect lattice). This paper focuses on the second regime, studying the far-field scattering of an incident wave due to defects, which is motivated by engineering problems such as damage detection and waveguide design.

In the context of mechanical waves, the dynamics of defective lattices has been studied in the setting of both localized modes and far-field scattering. Localized vibrations in the stop-band of the perfect lattice are investigated in the works of [8, 9, 10, 11, 12]. In the far-field setting, the study of elastic wave scattering has focused on simple discrete architectures with analytical dispersion relations [13, 14]. However, physically realizable metamaterial architectures typically exhibit complicated dispersion relations that must be numerically computed.

This paper develops a far-field scattering model for defective metamaterials that applies generally as long as the dispersion relations and corresponding mode shapes of the defect-free lattice are numerically available. Thus, it applies to a wide range of metamaterials whose dispersion relations are computable, for example, from a finite element model of a unit cell. In terms of the Bloch modes of the perfect lattice, our model captures how an incident wave is scattered due to localized defects taking the form of density perturbations.

The basis for the proposed scattering model is the lattice Green's function, which de-

scribes the response of a periodic lattice to a harmonic point excitation. While there is no general analytical solution for the lattice Green's function, its far-field asymptotics are attainable [15], enabling the analysis of scattering. We use Langley's approach for obtaining the far-field lattice Green's function in terms of a Bloch eigenmode expansion [16], which is applicable generally as long as dispersion relations and corresponding mode shapes are numerically available. However, the far-field lattice Green's function is singular at the origin, which poses a challenge for the analysis of point scatterers [17]. To circumvent this singularity, we employ the so-called *local perturbation method* [17, 18]. The local perturbation method assumes defects of finite size on a length scale much smaller than wavelengths of interest, and is valid for defects of arbitrary strength.

Two key features of our scattering model are its ability to capture strong defects and that it considers a periodic architecture, rather than a homogeneous solid, as the "background" material. Common scattering approximations often assume weak perturbations, such as the Born and Rytov approximations [19]. Alternatively, we consider potentially high-amplitude defects on a shorter length scale than the relevant wavelengths (i.e., restricting the length scale of a defect instead of its magnitude) – a setting that has enabled efficient and accurate multiple scattering analysis for one-dimensional elastic systems [20]. Specifically, we adopt the local perturbation method, which allows for arbitrary strength defects while regularizing the singular far-field lattice Green's function to enable a semi-analytical scattering framework. Additionally, while multiple scattering methods have been used to study metamaterials consisting of arrangements of scatterers attached to a homogeneous material [21, 22, 23], our approach considers scatterers embedded in a periodic material, enabling the analysis of a wide range of metamaterial architectures. We demonstrate our scattering model on a simple mass-spring network as well as a beam-based metamaterial, which agrees closely with high-fidelity transient simulations.

The proposed scattering model provides an alternative to high-fidelity modeling of wave scattering in defective metamaterials. As a semi-analytical modeling framework, it offers both the versatility to model metamaterials with arbitrary unit cells (defined by an FE model) and the efficiency to be used in inverse problems. For proof of concept, we demonstrate the inverse design of a set of defects embedded in a metamaterial to beam the wave emanating from a point source along one direction. Overall, the proposed model provides a foundation for pursuing challenging inverse problems from uncovering novel metamaterial functionalities through defect engineering to damage detection in metamaterials.

## 2. Preliminaries

We begin with an overview of wave motion in periodic elastic media, upon which a scattering model is built in subsequent sections.

### *2.1. Elastic waves in a periodic material*

Consider small-amplitude elastic waves in a continuum, governed by the elastodynamic equation

$$\frac{\partial}{\partial x_j}\left(C_{ijkl}\frac{\partial u_k}{\partial x_l}\right) + f_i = \rho \ddot{u}_i \tag{1}$$

where $\boldsymbol{u}(\boldsymbol{x},t) \in \mathcal{B}\times\mathbb{R}\to\mathbb{R}^d$ is the displacement vector, which is a function of spatial coordinate $\boldsymbol{x}\in\mathcal{B}$ and time $t$, defined for a body $\mathcal{B}\subset\mathbb{R}^d$ in $d$-dimensional space, and $\boldsymbol{f}(\boldsymbol{x},t)\in\mathcal{B}\times\mathbb{R}\to\mathbb{R}^d$ is a body force. The density $\rho(\boldsymbol{x})$ and elasticity tensor $\boldsymbol{C}(\boldsymbol{x})$ are periodic with unit cell $\Omega$. Einstein's summation convention is used throughout this paper. Assuming time-harmonic forcing $\boldsymbol{f}(\boldsymbol{x},t)=\boldsymbol{F}(\boldsymbol{x})e^{-\mathrm{i}\omega t}$ and displacement $\boldsymbol{u}(\boldsymbol{x},t)=\boldsymbol{U}(\boldsymbol{x})e^{-\mathrm{i}\omega t}$ with frequency $\omega$ yields the time-harmonic elastodynamic equation

$$\frac{\partial}{\partial x_j}\left(C_{ijkl}\frac{\partial U_k}{\partial x_l}\right)+\rho\omega^2U_i=-F_i. \tag{2}$$

Due to the periodicity of the material properties, we seek Bloch wave solutions of the form

$$\boldsymbol{U}=\tilde{\boldsymbol{U}}e^{\mathrm{i}\boldsymbol{k}\cdot\boldsymbol{x}} \tag{3}$$

where $\tilde{\boldsymbol{U}}(\boldsymbol{x})$ is a $\Omega$-periodic complex amplitude, and a real wave vector $\boldsymbol{k}\in\mathbb{R}^d$ is considered. Seeking solutions of this form, the elastodynamic equation becomes

$$\mathcal{L}^B[\tilde{\boldsymbol{U}}]+\omega^2\rho\tilde{\boldsymbol{U}}=-\boldsymbol{F} \tag{4}$$

where the *Bloch operator* $\mathcal{L}^B$ takes the form [24, 25]

$$\mathcal{L}^B_i[\tilde{\boldsymbol{U}}]=\frac{\partial C_{ijkl}}{\partial x_j}\left(\frac{\partial}{\partial x_l}+\mathrm{i}k_l\right)\tilde{U}_k+C_{ijkl}\left(\frac{\partial^2}{\partial x_l\partial x_j}+\mathrm{i}k_j\frac{\partial}{\partial x_l}+\mathrm{i}k_l\frac{\partial}{\partial x_j}-k_lk_j\right)\tilde{U}_k. \tag{5}$$

To obtain the dispersion relations of a periodic material, an eigenvalue problem is defined considering Eq. (4) over a unit cell in the absence of forcing. Typically, it cannot be solved analytically and numerical methods are employed to solve for the Bloch modes [26, 27].

For a given wave vector, mode $j$ consists of the eigenfrequency $\omega_j(\boldsymbol{k})$ and the eigenfunction $\boldsymbol{\psi}_j(\boldsymbol{x},\boldsymbol{k}):\Omega\times\mathbb{R}^d\to\mathbb{C}^d$, which corresponds to the mode shapes of the unit cell. The eigenfunctions are orthogonal with respect to the weighted inner product

$$\langle\boldsymbol{\psi}_i,\boldsymbol{\psi}_j\rangle=\int_\Omega\rho\boldsymbol{\psi}_i^*\boldsymbol{\psi}_j\,\mathrm{d}\boldsymbol{x} \tag{6}$$

and are defined to be mass-normalized such that

$$\langle\boldsymbol{\psi}_i,\boldsymbol{\psi}_j\rangle=\delta_{ij}. \tag{7}$$

Here, $()^*$ represents the complex conjugate and $\delta_{ij}$ is the Kronecker delta. Mass normalization of mode shapes simplifies in the definition of the lattice Green's function in Section 2.2.

Given the Bloch eigenmodes, a general function may be expressed using an eigenfunction expansion. For a function $\boldsymbol{h}(\boldsymbol{x})$, its *Bloch expansion* [28] takes the form

$$\boldsymbol{h}(\boldsymbol{x})=|\Omega_k|^{-1}\int_{\Omega_k}\sum_{j=1}^{\infty}\alpha_j(\boldsymbol{k})\boldsymbol{\psi}_j(\boldsymbol{x},\boldsymbol{k})e^{\mathrm{i}\boldsymbol{k}\cdot\boldsymbol{x}}\,\mathrm{d}\boldsymbol{k} \tag{8}$$

where $\alpha_j\in\mathbb{C}$ represents the modal amplitude of eigenfunction $\boldsymbol{\psi}_j(\boldsymbol{x},\boldsymbol{k})$, $\Omega_k$ represents the first Brillouin zone, and $|\Omega_k|$ is the volume of the first Brillouin zone. Note that $|\Omega_k|=$

$(2\pi)^d/|\Omega|$, where $|\Omega|$ is the volume of a unit cell in physical space. Due to the periodicity of the dispersion relations in $\boldsymbol{k}$-space, the Bloch expansion only needs to include modes in the first Brillouin zone, hence the integration over $\Omega_k$ in Eq. (8). The modal amplitudes of Eq. (8) may be written in terms of the given function $\boldsymbol{h}(\boldsymbol{x})$, taking the form

$$\alpha_j(\boldsymbol{k}) = \int_{\mathbb{R}^d} \rho(\boldsymbol{x})\boldsymbol{h}(\boldsymbol{x})e^{-\mathrm{i}\boldsymbol{k}\cdot\boldsymbol{x}}\boldsymbol{\psi}_j^*(\boldsymbol{x},\boldsymbol{k})\,\mathrm{d}\boldsymbol{x}. \tag{9}$$

The relation of the Bloch expansion to the plane wave expansion is discussed in [29]. Leveraging the Bloch expansion, a convenient form of the elastodynamic Green's function for a periodic lattice is obtained in the following.

### *2.2. Lattice Green's function*

The lattice Green's function captures the response of a periodic medium to a point harmonic forcing. Development of lattice Green's functions originally stems from the study of atomic lattices [3, 4, 30, 31]. Subsequently, extensions to mechanical waves have demonstrated lattice Green's functions as a tool for modeling dynamics of structural lattices [16, 32]. An analogous treatment of the lattice Green's function via Bloch expansions in photonics is presented in [33].

For elastic waves in a periodic material, the lattice Green's function $\boldsymbol{G}_n(\boldsymbol{x}-\boldsymbol{x}_0,\omega)$ represents the solution to Eq. (2) with a harmonic point force at point $\boldsymbol{x}_0$ along direction $\boldsymbol{e}_n$, where $n = 1$, 2, or 3 is the index of the axis along which the point force is aligned. Thus, the Green's function satisfies

$$\frac{\partial}{\partial x_j}\left(C_{ijkl}\frac{\partial G_{nk}}{\partial x_l}\right) + \rho\omega^2 G_{ni} = -\delta(\boldsymbol{x}-\boldsymbol{x}_0)e_{ni} \tag{10}$$

where $\delta(\boldsymbol{x}-\boldsymbol{x}_0)$ is the Dirac delta function. To simplify notation, we omit the explicit $\omega$-dependence of the Green's function in the remainder of our formulations. In terms of the Green's function, the displacement amplitude $\boldsymbol{U}$ due to an arbitrary forcing $\boldsymbol{F}$ is given by [34]

$$U_n(\boldsymbol{x}) = \int_{\mathbb{R}^d} G_{ni}(\boldsymbol{x}-\boldsymbol{x}')F_i(\boldsymbol{x}')\,\mathrm{d}\boldsymbol{x}'. \tag{11}$$

To obtain a useful form of the Green's function, we leverage the Bloch expansion. Writing $\boldsymbol{G}_n$ as an expansion of Bloch eigenfunctions yields

$$\boldsymbol{G}_n(\boldsymbol{x}) = |\Omega_k|^{-1}\int_{\Omega_k} \tilde{\boldsymbol{G}}_n e^{\mathrm{i}\boldsymbol{k}\cdot\boldsymbol{x}}\,\mathrm{d}\boldsymbol{k} \tag{12}$$

where

$$\tilde{\boldsymbol{G}}_n(\boldsymbol{x},\boldsymbol{k}) = \sum_{j=1}^{\infty}\alpha_j(\boldsymbol{k})\boldsymbol{\psi}_j(\boldsymbol{x},\boldsymbol{k}). \tag{13}$$

What remains is to obtain the coefficients $\alpha_j$. To this end, we define a Bloch expansion to capture the forcing term as

$$\rho^{-1}(\boldsymbol{x})\delta(\boldsymbol{x}-\boldsymbol{x}_0)\boldsymbol{e}_n = |\Omega_k|^{-1}\int_{\Omega_k}\tilde{\boldsymbol{F}}e^{\mathrm{i}\boldsymbol{k}\cdot\boldsymbol{x}}\,\mathrm{d}\boldsymbol{k}. \tag{14}$$

Upon denoting $\boldsymbol{\psi}_{j0} = \boldsymbol{\psi}_j(\boldsymbol{x}_0,\boldsymbol{k})$ as the mode shape evaluated at the excitation point, $\tilde{\boldsymbol{F}}$ may be written as

$$\tilde{\boldsymbol{F}}(\boldsymbol{x},\boldsymbol{k}) = \sum_{j=1}^{\infty}(\boldsymbol{\psi}_{j0}^{*}\boldsymbol{e}_n)\boldsymbol{\psi}_j e^{-\mathrm{i}\boldsymbol{k}\cdot\boldsymbol{x}_0}. \tag{15}$$

To arrive at Eq. (15), we have leveraged Eq. (9) and the sifting property of the delta function. Using Eqs. (12) and (14) together with the linearity of Eq. (10) leads to

$$\mathcal{L}^{B}[\tilde{\boldsymbol{G}}_n] + \omega^2\rho\tilde{\boldsymbol{G}}_n = -\rho\tilde{\boldsymbol{F}}. \tag{16}$$

Inserting Eqs. (13) and (15) in Eq. (16) yields

$$\sum_{j=1}^{\infty}\rho\alpha_j\boldsymbol{\psi}_j(\omega^2-\omega_j^2) = -\sum_{j=1}^{\infty}\rho\boldsymbol{\psi}_{j0}^{*}\boldsymbol{e}_n\boldsymbol{\psi}_j e^{-\mathrm{i}\boldsymbol{k}\cdot\boldsymbol{x}_0}. \tag{17}$$

After multiplying each side of Eq. (17) by $\boldsymbol{\psi}_k$, integrating over a unit cell, and applying the orthogonality condition of Eq. (7), we obtain an expression for the coefficients

$$\alpha_j = \frac{\boldsymbol{\psi}_{j0}^{*}\boldsymbol{e}_n e^{-\mathrm{i}\boldsymbol{k}\cdot\boldsymbol{x}_0}}{\omega_j^2-\omega^2}. \tag{18}$$

With coefficients $\alpha_j$ in hand, from Eqs. (12) and (13) the Bloch expansion representation of the lattice Green's function takes the form

$$\boldsymbol{G}_n(\boldsymbol{x}-\boldsymbol{x}_0) = \frac{|\Omega|}{(2\pi)^d}\int_{\Omega_k}\sum_{j=1}^{\infty}\frac{(\boldsymbol{\psi}_{j0}^{*}\boldsymbol{e}_n)\boldsymbol{\psi}_j e^{\mathrm{i}\boldsymbol{k}\cdot(\boldsymbol{x}-\boldsymbol{x}_0)}}{\omega_j^2-\omega^2}\,\mathrm{d}\boldsymbol{k}. \tag{19}$$

Eq. (19) represents the exact form of the lattice Green's function. Typically this integral form cannot be analytically evaluated. However, asymptotic analysis provides a platform for understanding its near- and far-field behavior. Generally, one can investigate the local "defect modes" arising near the defect that are outside of the spectrum of the perfect lattice [8] or the far-field behavior of how the perfect lattice modes are scattered by the defect [4, 16]. In this paper, we investigate the latter case concerning frequency $\omega$ within a pass-band of the perfect lattice, such that a pole is present in Eq. (19). While not considered here, we also note that asymptotic evaluation of the wave field, in both the near- and far-field regimes, is also possible when the excitation distribution is localized in the wave vector space [29].

### 2.3. Far-field asymptotics of the 2D lattice Green's function

Considering the case when the excitation frequency lies in a pass-band, the lattice Green's function integral of Eq. (19) may be evaluated asymptotically in the far-field limit using contour integration. Specifically, Lighthill [35] derived the far-field asymptotics of this form of integral by combining the residue theorem with the method of stationary phase, for both the two- and three-dimensional cases. In this work, we consider two-dimensional examples, so we limit our presentation of the far-field lattice Green's function to the two-dimensional case. However, Lighthill's original integration formulation for the 3D case is presented in [36], which was used in early derivations for the far-field Green's function in homogeneous anisotropic elastic solids [37].

To evaluate Eq. (19) in the far-field limit, we follow the integration scheme for the 2D case presented in Chapter 4 of [35], which is further discussed in the structural mechanics setting by Langley [16]. The resulting far-field asymptotic form of the lattice Green's function is

$$\boldsymbol{G}_n(\boldsymbol{x}-\boldsymbol{x}_0) = \frac{\mathrm{i}|\Omega|(\boldsymbol{\psi}_0^* \boldsymbol{e}_n)\boldsymbol{\psi}}{2\omega\sqrt{2\pi|Z|}} e^{-\mathrm{i}\frac{\pi}{4}\mathrm{sgn}(Z)} e^{\mathrm{i}\boldsymbol{k}\cdot(\boldsymbol{x}-\boldsymbol{x}_0)}. \tag{20}$$

In Eq. (20), the contribution of a single mode is considered and we omit the summation over modes and subscripts on $\omega$ and $\boldsymbol{\psi}$. If multiple dispersion branches present at the forcing frequency, their contributions should be summed. The quantity $Z$ is defined as

$$Z = \frac{\partial^2\omega}{\partial k_1^2}\frac{\partial\omega}{\partial k_2}(x_2 - x_{02}) - \frac{\partial^2\omega}{\partial k_1 \partial k_2}\left(\frac{\partial\omega}{\partial k_1}(x_2 - x_{02}) + \frac{\partial\omega}{\partial k_2}(x_1 - x_{01})\right) + \frac{\partial^2\omega}{\partial k_2^2}\frac{\partial\omega}{\partial k_1}(x_1 - x_{01}), \tag{21}$$

capturing the curvature of the dispersion surface. All quantities dependent on $\boldsymbol{k}$ in Eqs. (20) and (21) must be evaluated at a *stationary point*, which results from using the stationary phase method in the approximation of the integral of Eq. (19). Wave vector $\boldsymbol{k}$ corresponds to a stationary point if the group velocity $\boldsymbol{V} = \frac{\partial\omega}{\partial\boldsymbol{k}}$ evaluated at $\boldsymbol{k}$ is parallel to the vector $\boldsymbol{x} - \boldsymbol{x}_0$; see [16] for further discussion. Stationary points can be determined by solving for $\boldsymbol{k}$ that satisfies

$$V_1(x_2 - x_{02}) - V_2(x_1 - x_{01}) = 0, \tag{22}$$

so that the group velocity vector $\boldsymbol{V}(\boldsymbol{k})$ is aligned with the position vector. If there are multiple stationary points, which may occur if the isofrequency contour of the dispersion surface is non-convex, $\boldsymbol{G}_n$ is obtained by summing the evaluation of Eq. (20) over all stationary points. Without loss of generality, we focus on the case where there is only a single stationary point to simplify notation. Finally, we note that the far-field lattice Green's function of Eq. (20) is singular at $\boldsymbol{x} = \boldsymbol{x}_0$ since $Z$ becomes zero at that point, which warrants special treatment for use of the Green's function in the analysis of scattering.

## 3. Scattering due to a single defect

Based on the far-field lattice Green's function, we develop a framework for modeling elastic wave scattering due to defects. We consider defects that consist of density perturbations in a localized region defined by a length scale much smaller than the wavelengths of interest. To start, we develop the simplest case where only a single defect is present.

### 3.1. Problem setup

Consider modification of the density function of the periodic material such that the time-harmonic elastodynamic equation becomes

$$\frac{\partial}{\partial x_j}\left(C_{ijkl}\frac{\partial U_k}{\partial x_l}\right) + \omega^2\big(\rho(\boldsymbol{x}) + \hat{\rho}(\boldsymbol{x})\big)U_i = -F_i(\boldsymbol{x}). \tag{23}$$

The function $\hat{\rho}(\boldsymbol{x})$ represents a density perturbation to the otherwise perfect lattice with periodic density $\rho(\boldsymbol{x})$ and periodic elasticity tensor $\boldsymbol{C}(\boldsymbol{x})$. The term containing the perturbation may be interpreted as an additional forcing term, which allows for the solution to be expressed in terms of the Green's function, following Eq. (11). Thus, the solution for the scattered wave field in terms of the Green's function takes the form

$$U_n(\boldsymbol{x}) = \int_{\mathbb{R}^d} G_{ni}(\boldsymbol{x}-\boldsymbol{x}')F_i(\boldsymbol{x}')\,\mathrm{d}\boldsymbol{x}' + \omega^2\int_{\mathbb{R}^d} G_{ni}(\boldsymbol{x}-\boldsymbol{x}')\hat{\rho}(\boldsymbol{x}')U_i(\boldsymbol{x}')\,\mathrm{d}\boldsymbol{x}'. \tag{24}$$

At this point, we introduce simplifications to the problem setting, which are illustrated in Fig. 1a. Specifically, we consider an architected material that is periodic in two dimensions (in the $x_1x_2$-plane in Fig. 1a), so that the lattice Green's function of Eq. (20) is applicable. We further consider a point excitation in the $x_3$-direction, such that $\boldsymbol{F}(\boldsymbol{x}) = F\delta(\boldsymbol{x}-\boldsymbol{x}_0)\boldsymbol{e}_3$, and assume that out-of-plane deformations are de-coupled from in-plane deformations. This provides a simplification to the scattering problem since it results in scalar waves in the out-of-plane displacement field. This setting occurs, for example, in planar beam lattices where in- and out-of-plane modes are decoupled for the lower bands [38, 39]. We focus our formulations and examples in the remainder of the paper to this setting to simplify the resulting equations while maintaining a realistic problem setting that is experimentally feasible [40, 39]. For completeness, the general case of single scattering of vector-valued elastic waves is developed in Appendix A.

Assuming an out-of-plane point excitation that only excites out-of-plane waves, Eq. (24) simplifies to

$$U_3(\boldsymbol{x}) = G_{33}(\boldsymbol{x}-\boldsymbol{x}_0)F + \omega^2\int_{\mathbb{R}^d} G_{33}(\boldsymbol{x}-\boldsymbol{x}')\hat{\rho}(\boldsymbol{x}')U_3(\boldsymbol{x}')\,\mathrm{d}\boldsymbol{x}', \tag{25}$$

which relates the out-of-plane displacement amplitude $U_3$ to the $G_{33}$ component of the Green's function. Since the unknown displacement $U_3$ appears inside the second integral

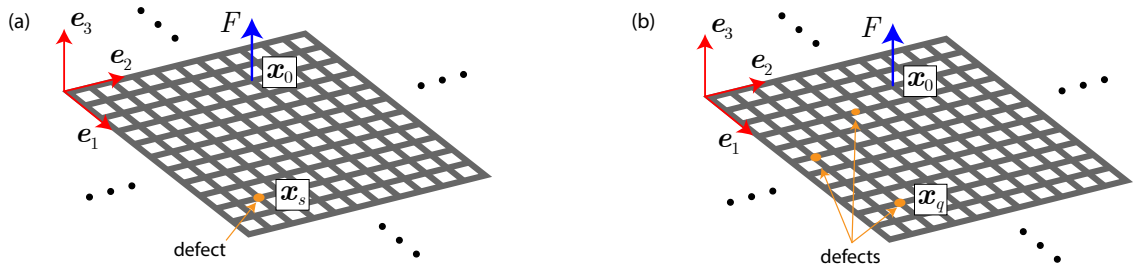


Figure 1: A planar beam lattice with defects that is subject to an out-of-plane point excitation. (a) Single defect case. (b) Multiple defects case. The orange regions represent density perturbation defects.

on the right-hand side, this is a nontrivial equation to solve. Unfortunately, the singularity at the origin in the far-field lattice Green's function of Eq. (20) does not allow consideration of a point defect at $\boldsymbol{x}_s$ of the form $\hat{\rho} = \hat{m}\delta(\boldsymbol{x} - \boldsymbol{x}_s)$ (where $\hat{m}$ is a constant equal to the total mass of the defect). To resolve the scattering system for a point defect requires evaluation of $G_{33}(\mathbf{0})$, which tends to infinity and prevents a straightforward scattering formulation [17].

We must turn to assumptions to resolve the singularity in the far-field lattice Green's function in order to solve the scattering problem. One approach is to regularize the Green's function by effectively filtering out short wavelengths, as discussed in [41] in the context of Maxwell's equations. However, there is not a unique way to impose a cutoff wavelength, making it difficult to attach physical meaning to such an approach. Alternatively, we adopt the so-called *local perturbation method*, which introduces physical arguments to circumvent the Green's function singularity [18]. See [17] for further discussion of point scatterer approximations in the context of singular Green's functions. Additional approaches for resolving Green's function singularities in scattering problems include matched asymptotic expansions [42] and, in some cases, cancellation of the singularity [43].

### *3.2. Local perturbation method for a single defect*

The local perturbation method assumes a finite sized defect on a length scale much smaller than the wavelength of interest. This method traces back to the work of Lifshitz [3, 4] in the context of atomic lattices and was further developed by Bass and coworkers [18, 44, 45]. Assigning a finite size to the defect allows for the Green's function singularity to be resolved, and the assumption that the defect length scale is smaller than the wavelength leads to a tractable solution to the scattering problem. Strikingly, there is no restriction on the strength of the defect. Furthermore, in our setting of periodic lattices with defects, there is no restriction on the length scale of the unit cell; long or short wavelengths with respect to the unit cell may be considered as long as the defect is much smaller than the wavelength.

In the local perturbation method, the defect is assumed to span a small but finite region of space, i.e., the support of the density perturbation function $\hat{\rho}(\boldsymbol{x})$ is small relative to the wavelength. This assumption corresponds to the assertion that the displacement field inside the defect is independent of the coordinates inside the defect. For a defect located in the vicinity of point $\boldsymbol{x}_s$, this corresponds to the approximation

$$\hat{\rho}(\boldsymbol{x})\boldsymbol{U}(\boldsymbol{x}) \approx \hat{\rho}(\boldsymbol{x})\boldsymbol{U}(\boldsymbol{x}_s). \tag{26}$$

The local perturbation method assumption of Eq. (26) leads to a key simplification of Eq. (25), which becomes

$$U_3(\boldsymbol{x}) = G_{33}(\boldsymbol{x} - \boldsymbol{x}_0)F + \omega^2 U_3(\boldsymbol{x}_s)\int_{\mathbb{R}^d} G_{33}(\boldsymbol{x} - \boldsymbol{x}')\hat{\rho}(\boldsymbol{x}')\,\mathrm{d}\boldsymbol{x}'. \tag{27}$$

Evaluating Eq. (27) at $\boldsymbol{x} = \boldsymbol{x}_s$ and solving for $U_3(\boldsymbol{x}_s)$ yields

$$U_3(\boldsymbol{x}_s) = \frac{G_{33}(\boldsymbol{x}_s - \boldsymbol{x}_0)F}{1 - \omega^2 \int_{\mathbb{R}^d} G_{33}(\boldsymbol{x}_s - \boldsymbol{x}')\hat{\rho}(\boldsymbol{x}')\,\mathrm{d}\boldsymbol{x}'}. \tag{28}$$

What remains is the evaluation of the integral appearing in the denominator, which we denote $I$, such that

$$I = \omega^2 \int_{\mathbb{R}^d} G_{33}(\boldsymbol{x}_s - \boldsymbol{x}')\hat{\rho}(\boldsymbol{x}')\,\mathrm{d}\boldsymbol{x}'. \tag{29}$$

The integrand of $I$ has a singularity at $\boldsymbol{x}' = \boldsymbol{x}_s$, but it is integrable on a finite domain. Performing this integration accounts for the shape of the defect. Practical aspects of defining this shape are discussed in the context of the examples in Section 5. For a given defect shape, evaluation of $I$ is presented in Appendix B.

Once $I$ is evaluated, the amplitude of the scattered displacement field is obtained via

$$U_3(\boldsymbol{x}) = G_{33}(\boldsymbol{x} - \boldsymbol{x}_0)F + \left[\frac{G_{33}(\boldsymbol{x}_s - \boldsymbol{x}_0)F}{1 - I}\right] \omega^2 \int_{\mathbb{R}^d} G_{33}(\boldsymbol{x} - \boldsymbol{x}')\hat{\rho}(\boldsymbol{x}')\,\mathrm{d}\boldsymbol{x}'. \tag{30}$$

The local perturbation assumption may be applied again, this time with the Green's function $G_{33}$ in place of $\boldsymbol{U}$ in Eq. (26). This is a reasonable assumption away from the singularity of the Green's function, i.e., as long as $\boldsymbol{x}$ is evaluated away from $\boldsymbol{x}_s$ in Eq. (30). As a result, Eq. (30) simplifies to

$$U_3(\boldsymbol{x}) = G_{33}(\boldsymbol{x} - \boldsymbol{x}_0)F + \left[\frac{G_{33}(\boldsymbol{x}_s - \boldsymbol{x}_0)F}{1 - I}\right] \omega^2 \int_{\mathbb{R}^d} \hat{\rho}(\boldsymbol{x}')\,\mathrm{d}\boldsymbol{x}' G_{33}(\boldsymbol{x} - \boldsymbol{x}_s). \tag{31}$$

The overall mass $\hat{m}$ of the perturbation corresponds to the integral of the perturbation density, given by

$$\hat{m} = \int_{\mathbb{R}^d} \hat{\rho}(\boldsymbol{x}')d\boldsymbol{x}'. \tag{32}$$

Finally, the scattered displacement amplitude is

$$U_3(\boldsymbol{x}) = G_{33}(\boldsymbol{x} - \boldsymbol{x}_0)F + \left[\frac{G_{33}(\boldsymbol{x}_s - \boldsymbol{x}_0)F}{1 - I}\right] \omega^2 \hat{m} G_{33}(\boldsymbol{x} - \boldsymbol{x}_s). \tag{33}$$

Eq. (33) provides direct means of evaluating the out-of-plane displacement field once the lattice Green's function and the integral $I$ are known, which is valid away from the excitation point $\boldsymbol{x}_0$ and the defect location $\boldsymbol{x}_s$.

## 4. Multiple scattering

We now extend the local perturbation scattering analysis to accommodate $N_s$ different localized defects at different points throughout the lattice, with the density perturbation corresponding to defect $q$ denoted by $\hat{\rho}_q(\boldsymbol{x})$. This leads to a governing time-harmonic elastodynamic equation of the form

$$\frac{\partial}{\partial x_j}\left(C_{ijkl}\frac{\partial U_k}{\partial x_l}\right) + \omega^2\left(\rho(\boldsymbol{x}) + \sum_{q=1}^{N_s}\hat{\rho}_q(\boldsymbol{x})\right)U_i = -F_i(\boldsymbol{x}). \tag{34}$$

Following Eq. (11), upon interpreting the density perturbation terms as forcing, the solution may be expressed in terms of the Green's function as

$$U_n(\boldsymbol{x}) = \int_{\mathbb{R}^d} G_{ni}(\boldsymbol{x}-\boldsymbol{x}')F_i(\boldsymbol{x}')\,\mathrm{d}\boldsymbol{x}' + \omega^2 \sum_{q=1}^{N_s} \int_{\mathbb{R}^d} G_{ni}(\boldsymbol{x}-\boldsymbol{x}')U_i(\boldsymbol{x}')\hat{\rho}_q(\boldsymbol{x}')\,\mathrm{d}\boldsymbol{x}'. \tag{35}$$

Eq. (35) holds for the general 3D case with arbitrary forcing. A simplified problem setting is again considered, consisting of a lattice periodic in two dimensions subject to an out-of-plane point force $\boldsymbol{F}(\boldsymbol{x}) = F\delta(\boldsymbol{x}-\boldsymbol{x}_0)\boldsymbol{e}_3$, as illustrated in Fig. 1b. We also assume that out-of-plane modes are decoupled from in-plane modes, as we did for the single scatterer case in Section 3.1. The resulting solution for the out-of-plane displacement simplifies to

$$U_3(\boldsymbol{x}) = G_{33}(\boldsymbol{x}-\boldsymbol{x}_0)F + \omega^2 \sum_{q=1}^{N_s} \int_{\mathbb{R}^d} G_{33}(\boldsymbol{x}-\boldsymbol{x}')U_3(\boldsymbol{x}')\hat{\rho}_q(\boldsymbol{x}')\,\mathrm{d}\boldsymbol{x}'. \tag{36}$$

Here, the overall scattered field $U_3$ appears on the right-hand side of Eq. (36), which captures the coupling between defects. However, one cannot directly solve Eq. (36) for $U_3$, so we must employ an approximation to obtain a tractable solution. One common approximation is the *first Born approximation* [46], where $U_3(\boldsymbol{x}')$ inside the integral of Eq. (36) is replaced with the incident field (in this case, the incident field would be $G_{33}(\boldsymbol{x}-\boldsymbol{x}_0)F$). The first Born approximation thus assumes small amplitude defects and weak scattering, eliminating coupling between defects. We do not adopt the Born approximation in this work. Instead, to evaluate the integral in Eq. (36), we turn to the local perturbation method. The local perturbation method assumes that the defects are on a length scale much shorter than the wavelength, which allows for a tractable solution to Eq. (36) while preserving coupling between defects, and hence *multiple scattering*.

### *4.1. Local perturbation method for multiple scattering*

Following a similar approach to the single scatterer case of Section 3.2, the local perturbation method is employed to resolve the integral in Eq. (36). Each of the defects is assumed to occupy a small region with respect to the wavelength such that Eq. (26) holds at the location of each defect.

Evaluating Eq. (36) at $\boldsymbol{x}_i$, the location of defect $i$, leads to

$$\begin{aligned} U_3(\boldsymbol{x}_i) =& G_{33}(\boldsymbol{x}_i-\boldsymbol{x}_0)F + \omega^2 U_3(\boldsymbol{x}_i)\int_{\mathbb{R}^d} G_{33}(\boldsymbol{x}_i-\boldsymbol{x}')\hat{\rho}_i(\boldsymbol{x}')\,\mathrm{d}\boldsymbol{x}' \\ &+ \omega^2 \sum_{\substack{q=1 \\ q\neq i}}^{N_s} \int_{\mathbb{R}^d} G_{33}(\boldsymbol{x}_i-\boldsymbol{x}')U_3(\boldsymbol{x}')\hat{\rho}_q(\boldsymbol{x}')\,\mathrm{d}\boldsymbol{x}'. \end{aligned} \tag{37}$$

Here, we have applied the local perturbation assumption of Eq. (26) to the isolated $i = q$ term to bring $U_3(\boldsymbol{x}_i)$ out of the integral. We define the local perturbation integral corresponding to defect $i$ as

$$I_i = \omega^2 \int_{\mathbb{R}^d} G_{33}(\boldsymbol{x}_i-\boldsymbol{x}')\hat{\rho}_i(\boldsymbol{x}')\,\mathrm{d}\boldsymbol{x}', \tag{38}$$

which is evaluated in Appendix B. The $q \neq i$ terms in Eq. (37) involve evaluation of the Green's function away from its singularity, where the defect may be treated as a point defect without issues due to the Green's function singularity, such that $\hat{\rho}_q(\boldsymbol{x}') = \hat{m}_q \delta(\boldsymbol{x}' - \boldsymbol{x}_q)$. It follows that Eq. (37) simplifies to

$$U_3(\boldsymbol{x}_i) = G_{33}(\boldsymbol{x}_i - \boldsymbol{x}_0)F + U_3(\boldsymbol{x}_i)I_i + \omega^2 \sum_{\substack{q=1 \\ q \neq i}}^{N_s} \hat{m}_q U_3(\boldsymbol{x}_q) G_{33}(\boldsymbol{x}_i - \boldsymbol{x}_q), \tag{39}$$

which can be recast in matrix form as

$$\begin{bmatrix} (1-I_1) & -\omega^2 \hat{m}_2 G(\boldsymbol{x}_1 - \boldsymbol{x}_2) & -\omega^2 \hat{m}_3 G(\boldsymbol{x}_1 - \boldsymbol{x}_3) & \dots \\ -\omega^2 \hat{m}_1 G(\boldsymbol{x}_2 - \boldsymbol{x}_1) & (1-I_2) & -\omega^2 \hat{m}_3 G(\boldsymbol{x}_2 - \boldsymbol{x}_3) & \dots \\ -\omega^2 \hat{m}_1 G(\boldsymbol{x}_3 - \boldsymbol{x}_1) & -\omega^2 \hat{m}_2 G(\boldsymbol{x}_3 - \boldsymbol{x}_2) & (1-I_3) & \dots \\ \vdots & \vdots & \vdots & \ddots \end{bmatrix} \begin{bmatrix} U_3(\boldsymbol{x}_1) \\ U_3(\boldsymbol{x}_2) \\ \vdots \\ U_3(\boldsymbol{x}_{N_s}) \end{bmatrix} = F \begin{bmatrix} G_{33}(\boldsymbol{x}_1 - \boldsymbol{x}_0) \\ G_{33}(\boldsymbol{x}_2 - \boldsymbol{x}_0) \\ \vdots \\ G_{33}(\boldsymbol{x}_{N_s} - \boldsymbol{x}_0) \end{bmatrix}. \tag{40}$$

Upon solving this system for the unknown displacements amplitudes $U_3(\boldsymbol{x}_i)$, the multiple scattering solution takes the form

$$U_3(\boldsymbol{x}) = G_{33}(\boldsymbol{x} - \boldsymbol{x}_0)F + \omega^2 \sum_{i=1}^{N_s} U_3(\boldsymbol{x}_i) \hat{m}_i G_{33}(\boldsymbol{x} - \boldsymbol{x}_i), \tag{41}$$

which is valid when evaluated away from defect locations $\boldsymbol{x}_i$ and the excitation location $\boldsymbol{x}_0$. This provides a framework for efficiently computing the scattered wave field, incorporating the interactions between the $N_s$ localized defects. We note that the linear system of Eq. (40) captures coupling between defects through its off-diagonal terms. Thus, multiple scattering effects are captured in the overall scattered displacement field computed in Eq. (41) through the displacements at the defect locations, $U_3(\boldsymbol{x}_i)$, which is the solution to the linear system of Eq. (40).

### *4.2. Numerical implementation procedure*

The formulations above enable efficient computation of the scattered elastic wave field in a periodic lattice with localized defects. An illustration of the resulting wave field computation framework is shown in Fig. 2, which is presented in the context of the multiple scattering case.

The process begins with the computation of dispersion relations for a periodic lattice without defects. Among the multiple approaches for dispersion relation computation [26], we utilize finite element analysis of a unit cell subject to Bloch boundary conditions. Based on the dispersion relations and corresponding mode shapes, Eq. (20) is evaluated to obtain the far-field lattice Green's function.

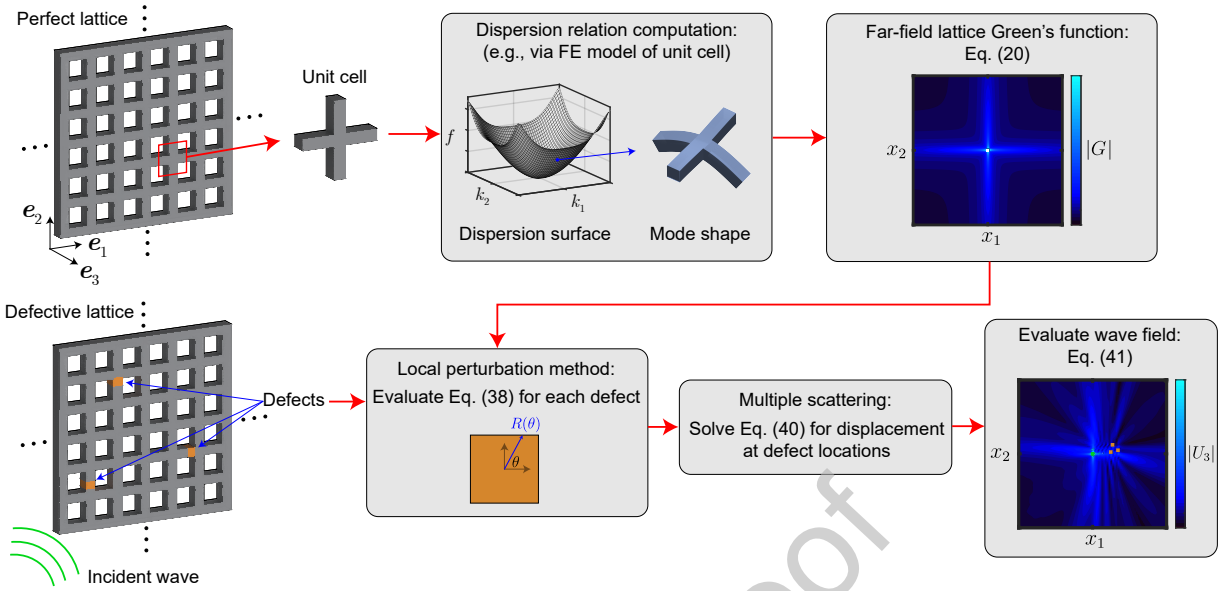


Figure 2: Pipeline for elastic wave field computation in a periodic lattice with localized defects.

With the lattice Green's function in hand, the defective lattice is analyzed. The first step is to evaluate the local perturbation integral of Eq. (38), following the procedure of Appendix B. Then, the multiple scattering system of Eq. (40) is constructed and solved for the displacements at the defect locations. Finally, the wave field at a given location follows from evaluating Eq. (41).

## 5. Forward modeling examples

To demonstrate the proposed scattering model, we present examples in the context of two architectures. The first is a mass-spring network, which provides a toy problem with an analytical dispersion relation. The second is a metamaterial with unit cells comprised of slender segments of elastic material, which are modeled as beams. For the beam-based metamaterial, dispersion relations are not analytically available and must be numerically computed, for which we use a finite element model of a unit cell. Based on the computed Bloch modes, the proposed scattering analysis is demonstrated.

### *5.1. Mass-spring network*

We first exemplify the scattering model on a simple mass-spring network. Consider an infinite two-dimensional square lattice with spacing $a$ consisting of particles connected by springs, as shown in Fig. 3a. Each mass has a single degree of freedom, the out-of-plane displacement $u$. All springs have stiffness $K$ and all particles have mass $m$ (except for the defective masses specified in the subsequent examples). The spring forces are proportional to the relative out-of-plane displacements of adjacent masses. This provides a simple setting for studying Bloch waves in a two-dimensional lattice and has been used in, e.g., [16] and [26].

The equation of motion for mass $(i, j)$ is

$$m\ddot{u}_{i,j} + 4Ku_{i,j} - K(u_{i-1,j} + u_{i+1,j}) - K(u_{i,j-1} + u_{i,j+1}) = 0. \tag{42}$$

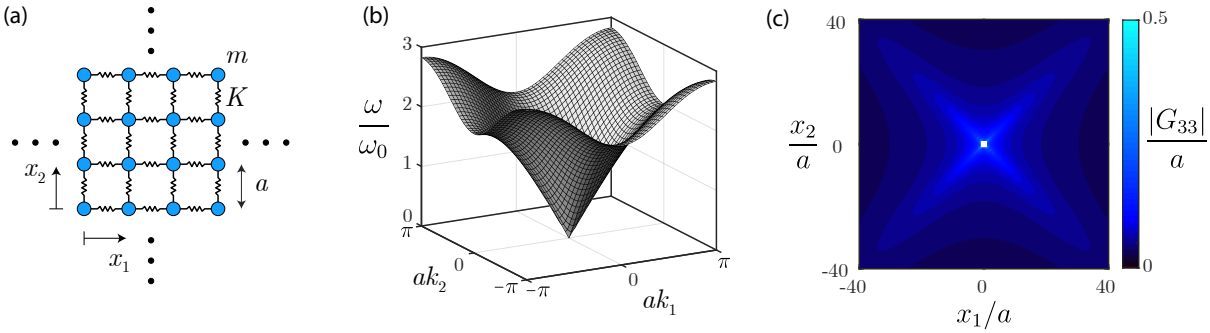


Figure 3: (a) Mass-spring network definition. (b) Dispersion relation. (c) Far-field lattice Green's function amplitude for $\omega = 1.75\omega_0$.

Dispersion relations corresponding to this equation of motion are available analytically, taking the form [26]

$$\omega(\boldsymbol{k}) = \omega_0\sqrt{2[2 - \cos(ak_1) - \cos(ak_2)]} \tag{43}$$

where $\omega_0 \equiv \sqrt{K/m}$. Fig. 3b shows a plot of the dispersion surface over the first Brillouin zone.

Given the dispersion relation, the far-field lattice Green's function follows from Eq. (20). For this example, the only relevant component of the Green's function is $G_{33}$, capturing the out-of-plane response to out-of-plane excitation. Fig. 3c shows the amplitude of $G_{33}$ corresponding to the frequency $\omega = 1.75\omega_0$. Note that $G_{33}$ is singular at the origin, which is why the value of $|G_{33}|$ at the origin is omitted in Fig. 3c.

*5.1.1. Single defect*

In the first example, a single defect is considered in an otherwise periodic mass spring network. The defective particle exhibits an added mass of $\hat{m} = 5m$ (such that its overall mass is $6m$) and has position $\boldsymbol{x}_s = (5a, 5a)$. Harmonic forcing of unit magnitude and frequency $\omega = 1.75\omega_0$ is applied to the mass at point $\boldsymbol{x}_0 = (0, 0)$. The corresponding mass-spring network is visualized in Fig. 4a.

To provide a reference solution, a transient simulation is performed by numerically solving the equations of motion of Eq. (42) on a finite grid of $300 \times 300$ unit cells. The simulation is terminated before the wave reflects off of the boundary. Fig. 4b plots the maximum displacement amplitude at each point during the simulation.

The proposed scattering model captures the solution by evaluating Eq. (33). To evaluate this equation, the quantities $G_{33}$ and $I$ must be determined. The Green's function $G_{33}$ (whose amplitude is shown in Fig. 3c) follows from evaluating Eq. (20) using the dispersion relations.

What remains is the evaluation of the local perturbation method integral $I$, which is discussed in Appendix B. To evaluate $I$, the shape of the mass perturbation must be defined. In this discrete setting, there is no distinct physical shape associated with the defect. However, a reasonable choice is to consider the defect to be a circle of diameter $a$, which is the smallest length scale associated with the mass-spring network. This choice leads to accurate results, though for discrete structures without a physically defined defect shape,

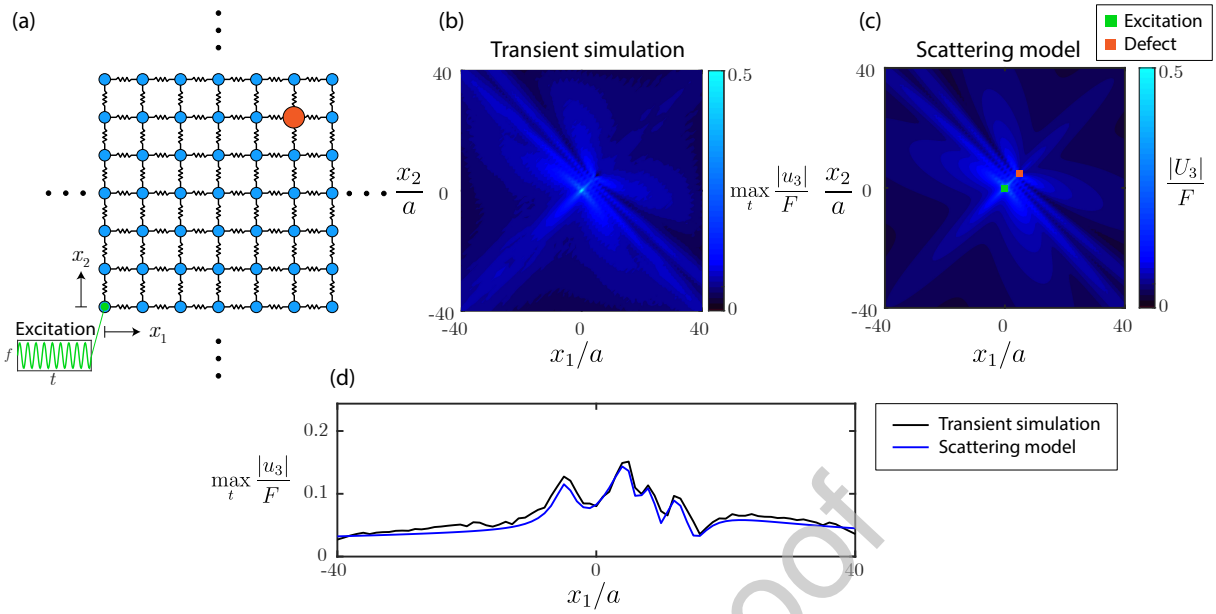


Figure 4: (a) Mass-spring example with a single defect. (b) Maximum displacement amplitude during the transient simulation. (c) Displacement amplitude from the scattering model. (d) Displacement amplitude along the $x_2 = -5a$ slice of plots (b) and (c).

the local perturbation method lacks a direct physical interpretation and instead acts as a regularization of the Green's function singularity.

In Fig. 4c, the displacement amplitude predicted by the scattering model from Eq. (33) is plotted on a $80a \times 80a$ domain. A slice of the displacement amplitude along the line $x_2 = -5a$ is shown in Fig. 4d. While the scattering model agrees closely with the transient simulation results, discrepancies arise due to two reasons. First, the local perturbation model is an approximation, and the corresponding assumptions introduce some error. Second, while the transient simulation has a harmonic forcing, additional frequency content is excited inherently as the lattice starts from rest. This is in contrast to the scattering model, which evaluates the response at a specific pure frequency.

For further comparison across different frequencies, an additional transient simulation was performed with broadband force excitation at the origin in the form of a linear chirp from $\omega = 0.1\omega_0$ to $\omega = 2\omega_0$. The amplitude of the frequency response function $U_3/F$ is plotted in Fig. 5 at three spatial locations, which is compared to the frequency response function amplitude predicted by the scattering model at the corresponding points. Close agreement is observed across most frequencies. Even at the location $(x_1 = 5a, x_2 = 4a)$ in Fig. 5a, which is one unit away from the defective mass, surprisingly close agreement is observed despite the fact that the scattering model is built upon far-field assumptions. At all points, increased discrepancy is observed approaching $\omega = 2\omega_0$, which corresponds to a *caustic*, where the curvature of the isofrequency contour is zero and therefore $Z = 0$, invalidating the far-field lattice Green's function of Eq. (20). See [35, 16] for further discussion of caustics.

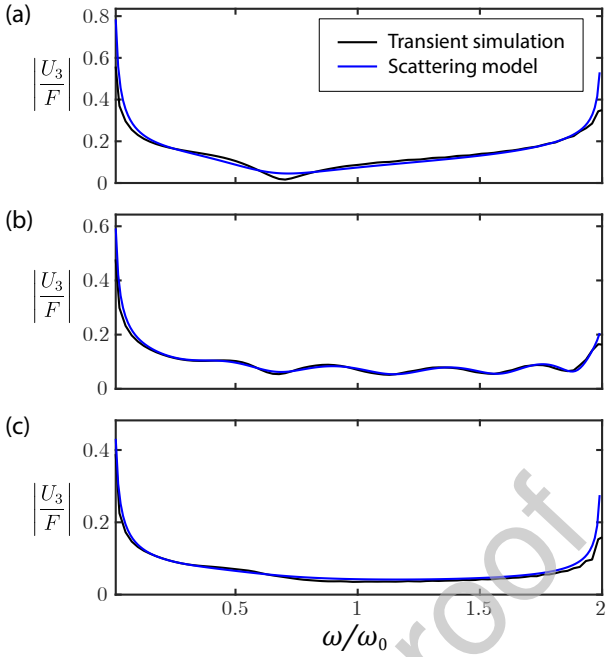


Figure 5: Broadband comparison between the transient simulation and scattering model for the single scatterer case of Fig. 4a. The frequency response function from both models is plotted at the spatial locations (a) $x_1 = 5a$, $x_2 = 4a$; (b) $x_1 = -10a$, $x_2 = 5a$; and (c) $x_1 = 15a$, $x_2 = 15a$.

### *5.1.2. Multiple defects*

To demonstrate the multiple scattering case, a second example is presented where three defects are present. The three defects at locations $\boldsymbol{x}_1 = (2a, 2a)$, $\boldsymbol{x}_2 = (0, 7a)$, and $\boldsymbol{x}_3 = (-2a, 2a)$ exhibit mass perturbations of $\hat{m}/m = -0.5$, 10, and 1, respectively. Harmonic forcing of unit magnitude and frequency $\omega = 1.5\omega_0$ is applied to the mass at point $\boldsymbol{x}_0 = (0, 0)$. The corresponding mass-spring network is illustrated in Fig. 6a. For comparison, a transient simulation is performed with the same parameters as in Section 5.1.1, except for the differing defects. The maximum displacement amplitude at each point in the transient simulation is shown in Fig. 6b.

The multiple scattering approximation for the displacement amplitude involves first the evaluation of Eq. (40) to solve for the amplitude at each defect, for which we use the same defect shape as in Section 5.1.1. Then, the result is inserted into Eq. (41) to evaluate the displacement amplitude at an arbitrary point. Figure 6c shows the displacement amplitude from the scattering analysis. Close agreement is evident between the multiple scattering model and the transient simulation, which is further exemplified by plotting the displacements along the line $x_2 = -5a$ in Fig. 6d.

To provide a comparison across frequencies, a broadband transient simulation was performed with the same parameters as discussed in Section 5.1.1. In Fig. 7, the frequency response function amplitude is plotted for both models at three spatial locations. Again, close agreement between the multiple scattering model and transient simulation is observed across frequencies, even in the near-field (Fig. 7a). Near the caustic at $\omega = 2\omega_0$, the scattering solution loses accuracy as the far-field evaluation of the lattice Green's function loses validity.

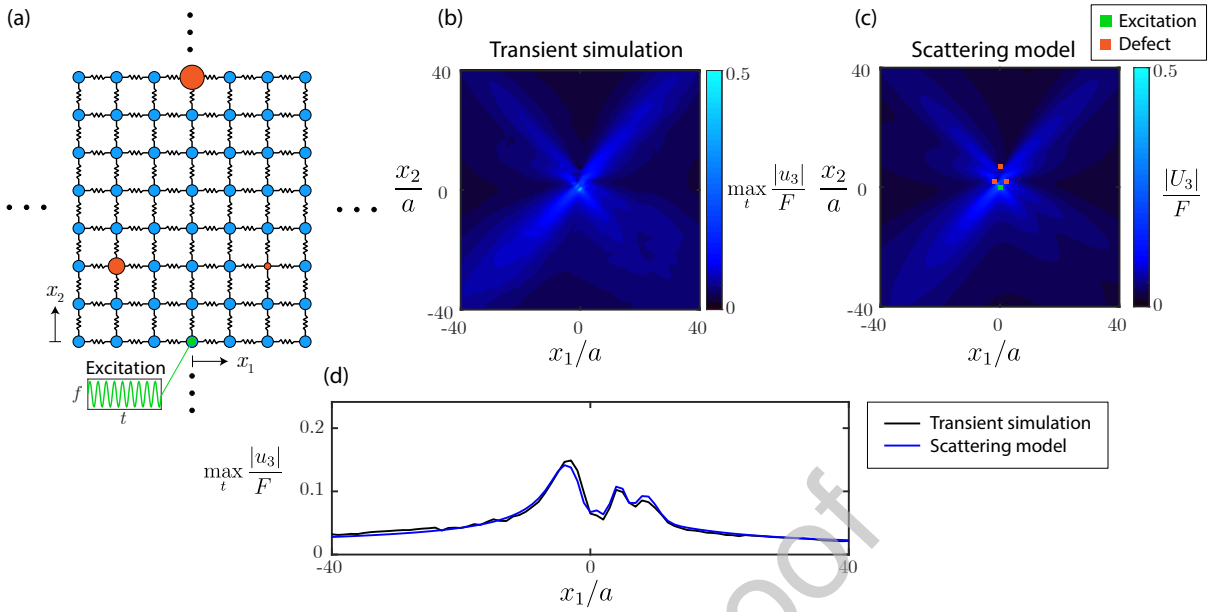


Figure 6: (a) Mass-spring example with three defects. (b) Maximum displacement amplitude during the transient simulation. (c) Displacement amplitude from the scattering model. (d) Displacement amplitude along the $x_2 = -5a$ slice of plots (b) and (c).

### *5.1.3. Disorder*

As the final example involving a mass-spring network, we demonstrate the scattering model as an efficient tool for modeling disordered metamaterials. A mass-spring network with 20 perturbations placed randomly within the region $1 \leq x_1/a \leq 15$, $1 \leq x_2/a \leq 15$. The mass perturbation of each defect is randomly selected from a uniform distribution on $-1 < \hat{m}/m < 2$. Harmonic forcing of unit magnitude and frequency $\omega = \omega_0$ is applied to the mass at point $\boldsymbol{x}_0 = (0, 0)$. Figure 8a illustrates the resulting architecture, where the orange masses are defective and their size is plotted proportionally to their total mass. Positions and mass perturbation values for each defect are listed in Appendix C.

A transient simulation provides a reference solution, with an analogous setup as discussed in Sections 5.1.1 and 5.1.2. The maximum displacement amplitude during the transient simulation as a function of position is shown in Fig. 8b.

The multiple scattering model solution for displacement amplitude is shown in Fig. 8c, which is calculated in the same fashion as for the example in Section 5.1.2, except with 20 defects. A slice of the displacement amplitude along the line $x_2 = -5a$ is shown in Fig. 8d. Again, there is close agreement between the transient simulation and the multiple scattering model. Thus, the proposed scattering model shows promise as a tool for characterizing and exploring the dynamics of disordered metamaterials.

Additionally, a broadband transient simulation was performed with the same parameters as discussed in Section 5.1.1. In Fig. 9, the frequency response function amplitude is plotted for both models at three spatial locations. Close agreement is again observed between the multiple scattering model and transient simulation across frequencies, including in the near-field (Fig. 7a), while the scattering solution loses accuracy approaching the caustic at $\omega = 2\omega_0$.

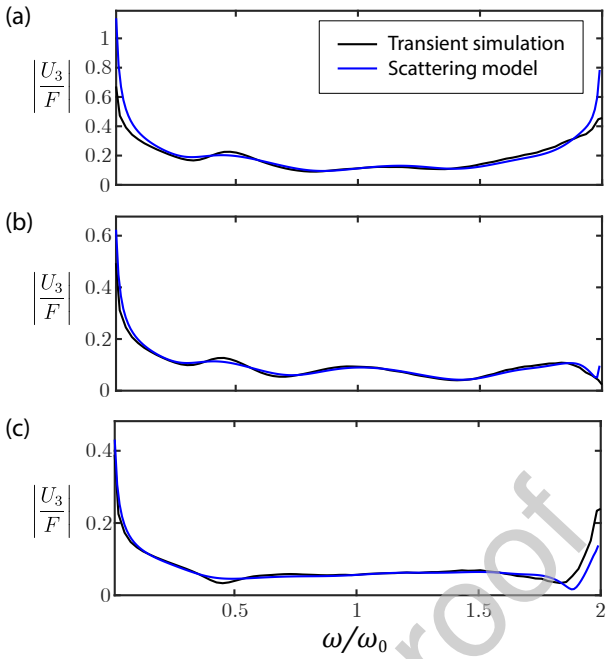


Figure 7: Broadband comparison between the transient simulation and scattering model for the three-defect case of Fig. 6a. The frequency response function from both models is plotted at the spatial locations (a) $x_1 = 0$, $x_2 = 3a$; (b) $x_1 = 10a$, $x_2 = 0$; and (c) $x_1 = 15a$, $x_2 = 15a$.

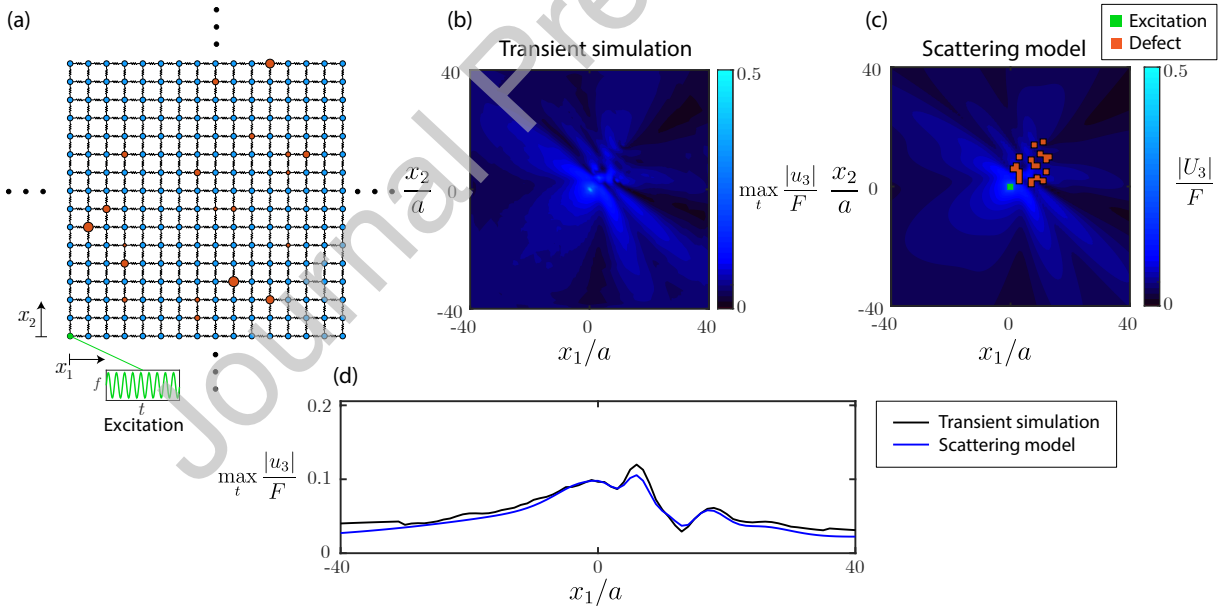


Figure 8: (a) Mass-spring example with 20 randomly placed defects. (b) Maximum displacement amplitude during the transient simulation. (c) Displacement amplitude from the scattering model. (d) Displacement amplitude along the $x_2 = -5a$ slice of plots (b) and (c).

### *5.2. Beam-based metamaterial*

To move beyond the setting of mass-spring networks, we present examples studying an architected material composed of elastic beams. A planar square lattice is considered, as

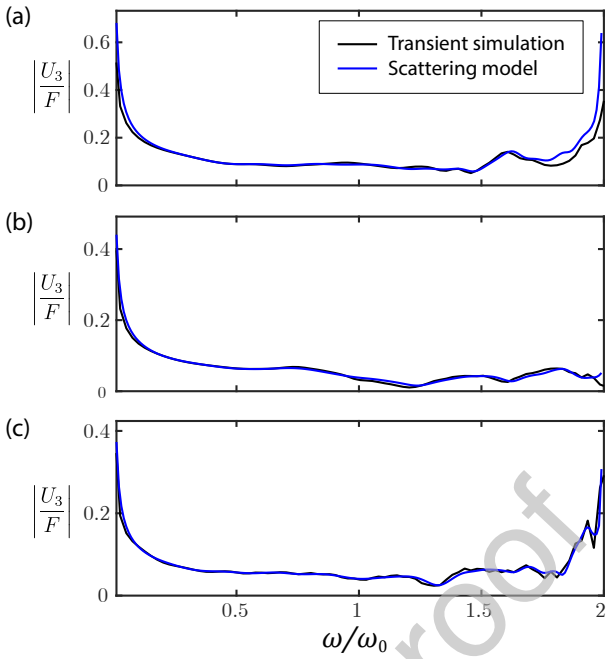


Figure 9: Broadband comparison between the transient simulation and scattering model for the disordered case of Fig. 8a. The frequency response function from both models is plotted at the spatial locations (a) $x_1 = 6a$, $x_2 = 6a$; (b) $x_1 = 20a$, $x_2 = 0$; and (c) $x_1 = 20a$, $x_2 = -20a$.

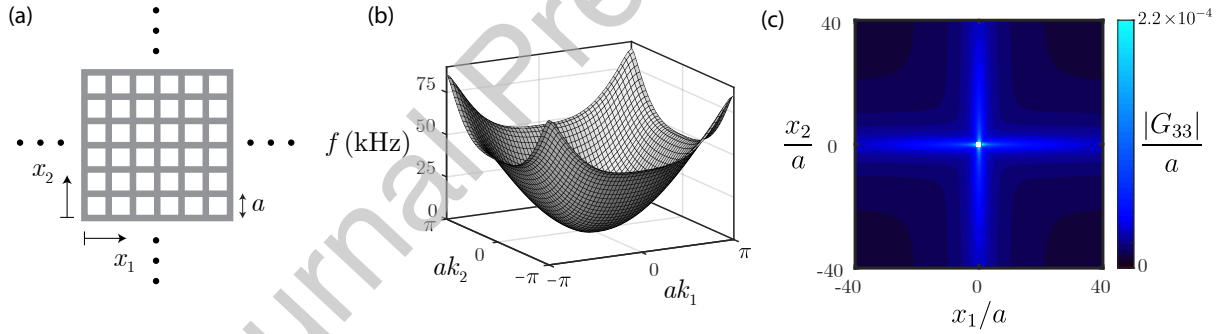


Figure 10: (a) Periodic beam lattice. (b) The first out-of-plane dispersion surface and (c) its contribution to the far-field lattice Green's function amplitude for $f = 40$ kHz.



illustrated in Fig. 10a. For planar beam lattices, the lowest out-of-plane modes are decoupled from the in-plane modes, allowing for the simplifications discussed in Section 3.1 to apply, reducing the scattering problem to scalar waves in the out-of-plane displacement. However, unlike the mass-spring network, this provides a physically realistic setting that can be realized experimentally [39, 40].

The dispersion relations of the beam-based metamaterial are not analytically available and they must be evaluated numerically. A finite element model of a unit cell is used to compute dispersion relations of the perfectly periodic lattice, following the standard approach presented in [47]. We model a unit cell with Timoshenko beam finite elements, which provide an efficient model for beam-based architectures that reliably captures the lowest dispersion branches. Alternatively, three-dimensional solid elements could be used to model a unit cell,

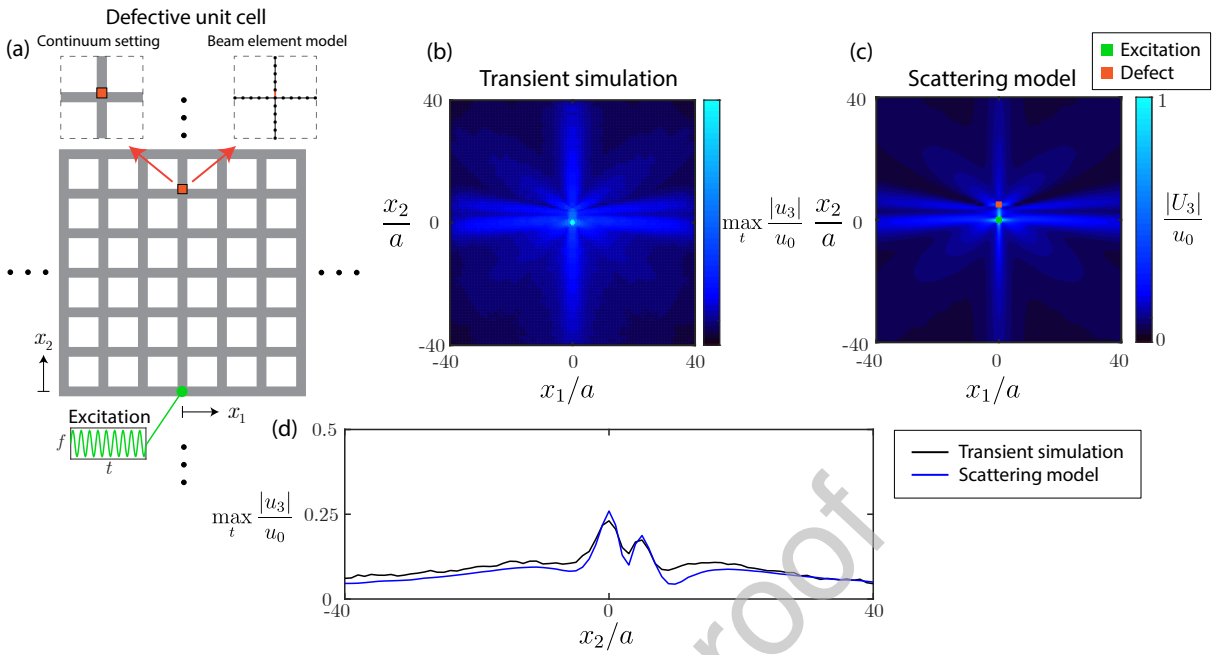


Figure 11: (a) Beam lattice example with one defect, with the defective unit cell highlighted. In the continuum setting, the defect is a square region of increased density, which is captured in the beam model by modifying the density of a single element. (b) Maximum displacement amplitude during a transient finite element simulation. (c) Displacement amplitude from the scattering model. (d) Displacement amplitude along the $x_1 = -20a$ slice of plots (b) and (c).

trading computational efficiency for accuracy of the higher modes. As discussed in [39], the lowest dispersion surfaces computed by Timoshenko beam element models agree closely with solid element-based models and experiments.

In the subsequent examples, dimensions are considered to match the experimental setting of [39]: the unit cell has side length $a = 5$ mm, the out-of-plane thickness is $T = 1$ mm, and the width of the beams is $b = 0.5$ mm. Nominal material properties of aluminum are used, with Young's modulus $E = 69$ GPa, Poisson's ratio $\nu = 1/3$, and density $\rho = 2700$ kg/m$^3$. Dispersion relations are computed using a Timoshenko beam element model of a unit cell with maximum element length of $a/10$, which was found to be sufficiently refined to accurately capture the lowest out-of-plane dispersion surface. All finite element computations are performed using the *ae108* code [48]. Fig. 10b shows the first out-of-plane dispersion surface plotted on the first Brillouin zone and Fig. 10c plots the far-field lattice Green's function at 40 kHz.

To compute the far-field lattice Green's function from Eq. (20), the group velocity as well as the second derivatives of the dispersion surface with respect to the wave vector components are needed. Before approaching the scattering problem, we pre-compute these derivatives on a grid spanning the first Brillouin zone using finite differences. Then, when evaluating the Green's function at an arbitrary wave vector, the dispersion surface derivatives are obtained by interpolation from the pre-computed values.

*5.2.1. Single defect*

We first consider an example where the beam lattice has a single defect. The defect is located at the point $\boldsymbol{x}_s = (0, 5a)$ and has an added mass of $\hat{m} = 2m_u$, where $m_u = 2abT$ is the overall mass of one unit cell. The defect is defined as a square region of side length $a/10$ with constant density. Harmonic excitation of unit magnitude and frequency $f = 40$ kHz is applied to the mass at point $\boldsymbol{x}_0 = (0, 0)$ in the out-of-plane direction. The corresponding beam lattice is illustrated in Fig. 11a.

To provide a reference for comparison, a transient dynamic finite element simulation is performed on a finite domain. The transient simulation uses Timoshenko beam finite elements with an element length of $a/10$ to mesh a domain of $100 \times 100$ unit cells. The defect is modeled by increasing the density of a single element. Fig. 11a illustrates a continuum unit cell with a square defect, as well as the corresponding beam element model. For excitation, a harmonic out-of-plane displacement is applied to the node at the center of the domain, which is taken as the origin. Displacement excitation is used because the alternative of applying an out-of-plane harmonic force to a planar beam lattice initially at rest leads to significant parasitic low-frequency content in the response [38]. Thus, displacement excitation provides a cleaner reference for comparison to the scattering model. The transient response is computed using Newmark-beta integration and the simulation is terminated before the wave hits the boundaries to avoid reflections. The maximum out-of-plane displacement at each point during the simulation is plotted in Fig. 11b.

The scattering model solution is computed by evaluating Eq. (33), which first requires evaluation of $G_{33}$ and $I$. To obtain $G_{33}$, Eq. (20) is evaluated using the pre-computed dispersion relation and dispersion relation derivatives. To obtain the local perturbation method integral $I$ of Eq. (29), the procedure outlined in Appendix B is followed considering the defect occupies a square region. The resulting displacement field predicted by the scattering model is plotted in Fig. 11c. A slice of the maximum displacements along $x_1 = -20a$ is plotted in Fig. 11d. The plotted displacements are normalized by the maximum displacement amplitude in each respective model, denoted by $u_0$.

The scattering model shows clear agreement with the transient simulation, capturing the features of the scattered wave field. Similar to the mass-spring network examples, discrepancies arise both due to the approximate nature of the scattering model and the fact that the transient simulation contains frequency content beyond a single frequency.

*5.2.2. Multiple defects*

For the final example, we model a beam lattice with multiple defects. Five defects are placed at points $\boldsymbol{x}_1 = (-5a, 0)$, $\boldsymbol{x}_2 = (-5a, 5a)$, $\boldsymbol{x}_3 = (0, 5a)$, $\boldsymbol{x}_4 = (5a, 5a)$, and $\boldsymbol{x}_5 = (5a, 0)$, each with added mass $\hat{m}_i = 5m_u$. Harmonic out-of-plane excitation is applied to the origin at $f = 20$ kHz. A transient simulation is performed for comparison, with the same setup as in the example of Section 5.2.1. Transient simulation results are shown in Fig. 12b.

The multiple scattering solution is determined by first solving Eq. (40) for the displacement at the defect locations, which are then used to evaluate Eq. (41). The quantities $G_{33}$ and $I_i$ are evaluated using the same process as described in Section 5.2.1. Fig. 12c shows the displacement amplitudes predicted by the scattering model, closely matching the transient simulation results. Finally, Fig. 12d compares the transient simulation and scattering model along $x_2 = -20a$, showing agreement between models.

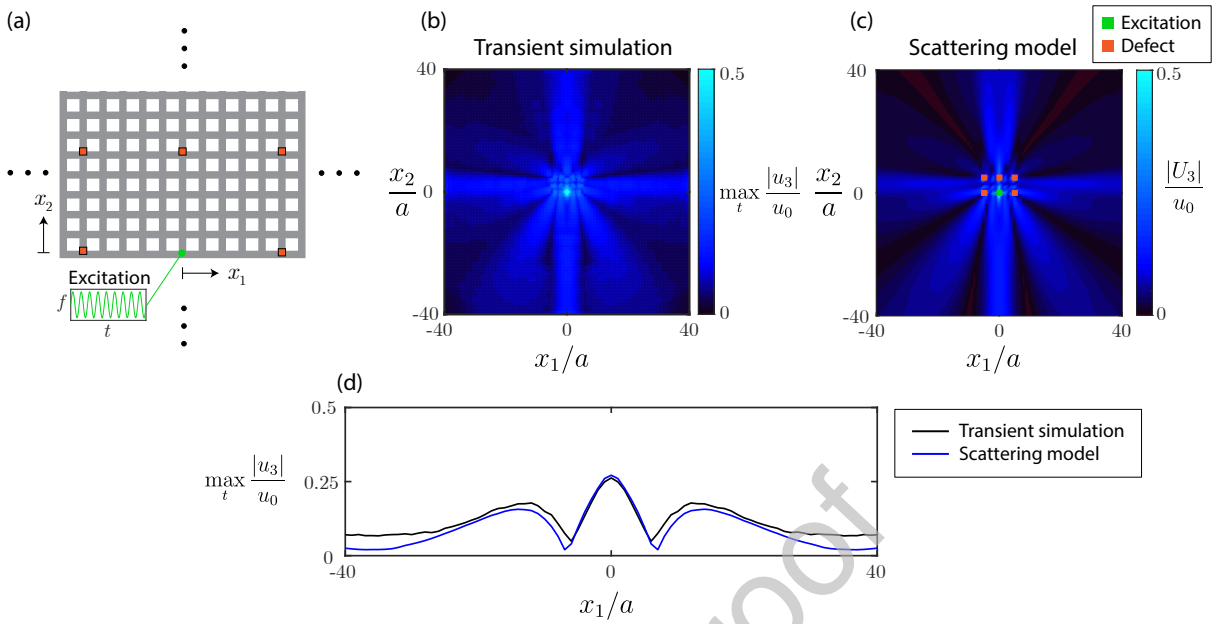


Figure 12: (a) Beam lattice example with 5 defects. (b) Maximum displacement amplitude during a transient simulation. (c) Displacement amplitude from the scattering model. (d) Displacement amplitude along the $x_1 = -20a$ slice of plots (b) and (c).

### *5.2.3. Computation time*

The presented semi-analytical scattering model offers a computationally efficient means of modeling defective periodic lattices. In the context of the beam-based metamaterial example of Section 5.2.1 with a single defect, the scattering model took 5.9 seconds to compute the displacement amplitude at 1600 points, on a 40×40 grid to produce Fig. 11c (excluding the computation time to pre-compute the dispersion relations). In contrast, the transient finite element model had 215,736 elements and took 18.0 minutes to run the simulation to produce Fig. 11b. For the multiple scattering case of Section 5.2.2 took 10.8 seconds to run while the FE model took 26.9 minutes, to produce Fig. 12c and b, respectively. We note that the scattering model was implemented in Matlab, while the transient FE simulations were performed in parallel in *ae108*, an open-source finite element code implemented in C++ [48].

In addition to its efficiency, the scattering model can be evaluated at a single point independently (unlike the transient FE simulations requiring a large domain to be modeled). This is particularly advantageous for inverse problems that concern the response at a small number of points, an example of which is given in Section 6.

## 6. Inverse design

We demonstrate the utility of the presented scatting model in the context of an inverse design problem. An optimization problem is considered for designing the magnitude of a set of $n_s$ mass perturbations at fixed locations to maximize the displacement amplitude at a prescribed point. The corresponding optimization problem takes the form

$$\max_{\hat{\boldsymbol{m}}} \mathcal{C} \tag{44}$$

where

$$\mathcal{C} = \frac{1}{2}|U_3(\boldsymbol{x}_t)|^2. \tag{45}$$

The design variable $\hat{\boldsymbol{m}} = [\hat{m}_1, ..., \hat{m}_{n_s}]$ is a vector of mass perturbation magnitudes corresponding to defects at a fixed set of locations $\boldsymbol{x}_i$ with $i = 1, ..., n_s$, and $\boldsymbol{x}_t$ is the target point at which we aim to maximize the displacement amplitude.

We specifically consider design of the mass-spring network studied in Section 5.1 with 64 defective masses located on a regular grid spanning $x_1 = \pm 14a$ and $x_2 = \pm 14a$, which correspond to the orange masses in Fig. 13a. An excitation frequency of $\omega = \omega_0$ is considered, and bounds are placed on the design variables such that $-0.8 \leq \hat{m}_i/m \leq 5$. The target point at which we aim to maximize amplitude is $\boldsymbol{x}_t = (0, 25a)$.

Gradient-based optimization is used to compute an optimal design. The gradient of the cost function with respect from the design variable, $\mathrm{d}\mathcal{C}/\,\mathrm{d}\hat{\boldsymbol{m}}$, is analytically available by differentiating Eq. (41) evaluated at $\boldsymbol{x}_t$. We use the NLopt implementation [49] of the L-BFGS algorithm [50] to perform the optimization. Since this is a nonconvex optimization problem, there is no guarantee the presented solution is a global minimum. However, we found that local gradient-based optimization was sufficient to find interesting solutions clearly demonstrating the objective of the inverse problem.

Fig. 13a shows the mass distribution of the optimal solution, where the plotted size of each defective mass is proportional to its overall mass $m + \hat{m}_i$. The full-field solution corresponding to the optimal design is shown in Fig. 13b and c, which are computed based a transient simulation and the scattering model, respectively. The solution demonstrates strong wave beaming toward the target point $\boldsymbol{x}_t$. Meanwhile, the displacements remain small in all other regions outside of the grid of defects, as the defects redirect as much energy as possible toward the target point.

This example demonstrates that defect engineering is a powerful means of tailoring wave propagation in metamaterials. However, we only scratch the surface of a vast design space of defects. We anticipate the computational tools presented in this paper will enable exploration of further regions of this design space to uncover new wave manipulation functionalities. Recent research on inverse scatterer design has explored objectives such as wave field design [51] and frequency dependent focusing [52] in the context of homogeneous elastic plates with embedded scatterers (as opposed to the periodic lattices with embedded scatterers studied here). Thus, future work could pursue a wide range of design objectives for the defective periodic lattice case, with potential for introducing additional design freedom since the unit cell of the periodic background material can be arbitrarily defined in our modeling framework.

## 7. Conclusion

We have presented a semi-analytical multiple scattering formulation for elastic wave propagation in periodic materials with defects. Unlike typical multiple scattering models, we consider the background material to be a periodic elastic lattice rather than a homogeneous material, which allows for a wide range of metamaterial architectures to be considered. Furthermore, the defects may be of arbitrary magnitude and shape; we only assume that their length scale is small relative to the wavelength.

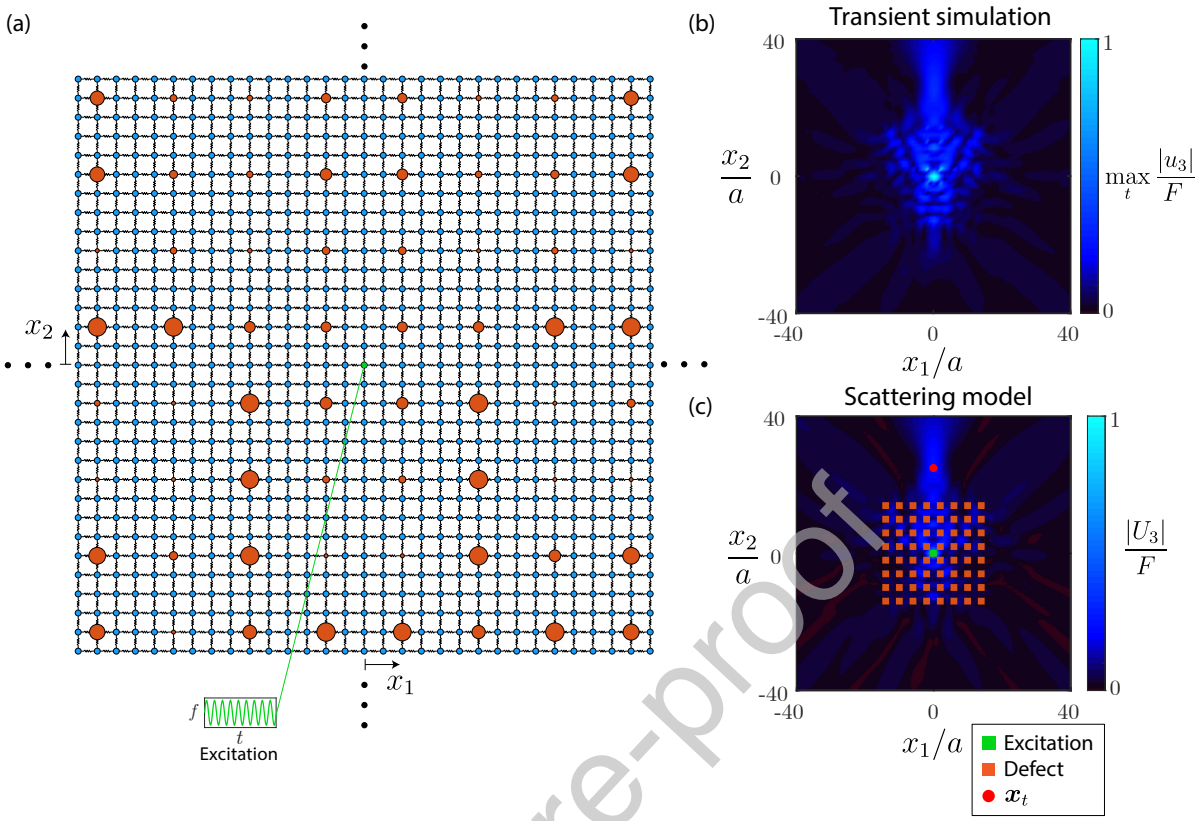


Figure 13: Inverse design of a set of defective masses in a mass-spring network. (a) Optimal solution, where the defective masses are plotted in orange with their size proportional to their overall mass. (b) Maximum displacement amplitude during a transient simulation of the optimal design. (c) Displacement amplitude of the optimal design computed using the scattering model.

The basis for this framework is the lattice Green's function evaluated asymptotically in the far field. By expressing the Green's function in terms of a Bloch mode expansion, the results apply generally to cases when the dispersion relations are available either analytically or numerically. Based on the Green's function, a scattering model is formulated under the assumption that defects are small relative to the wavelengths of interest; under this assumption, the local perturbation method enables straightforward evaluation of the scattered wave field. The resulting scattering model provides an efficient tool for computing the far-field response of wave scattering due to localized, but arbitrary magnitude defects in a metamaterial. We demonstrated close agreement between the scattering model and transient dynamic simulations in the setting of a mass-spring network and a beam-based metamaterial.

A key appeal of the proposed approach is that extremely complex geometries are efficiently modeled, such as metamaterial architectures with complicated unit cells and randomly distributed defects. It therefore lays a foundation for approaching inverse problems that cannot be solved with inefficient high-fidelity simulations (e.g., the transient finite element modeling used for comparison in this work). We demonstrate the inverse design of a set of defects in a mass-spring network to guide the wave emanating from a point excitation along one direction, providing an example of defect engineering for wave manipulation. Fu-

ture research developing extensions of this modeling framework to alternative defect types, such as perturbations to the geometry and constitutive model, would make progress toward tackling novel inverse problems from defect engineering to damage detection.

## Appendix A. Local perturbation method for the general 3D case

To motivate the examples of Section 5 and simplify notation, the main text focuses on the case when out-of-plane deformation is decoupled from in-plane deformation. This results in simplified scalar equations for the scattering analysis, while still capturing a physically realistic problem setting. For completeness, this appendix outlines the local perturbation method for a single scatterer in the general case when out-of-plane deformation is not decoupled from in-plane deformation. Additionally, we consider forcing $\boldsymbol{F}(\boldsymbol{x})$ in an arbitrary direction, resulting in vector-valued waves in the displacement field.

Starting from general solution in terms of the Green's function of Eq. (24), applying the local perturbation method assumption of Eq. (26) results in

$$U_n(\boldsymbol{x}) = \int_{\mathbb{R}^d} G_{ni}(\boldsymbol{x} - \boldsymbol{x}')F_i(\boldsymbol{x}')\,\mathrm{d}\boldsymbol{x}' + \omega^2 U_i(\boldsymbol{x}_s)\int_{\mathbb{R}^d} G_{ni}(\boldsymbol{x} - \boldsymbol{x}')\hat{\rho}(\boldsymbol{x}')\,\mathrm{d}\boldsymbol{x}'. \tag{A.1}$$

Evaluating the displacement at the defect location $\boldsymbol{x}_s$ yields

$$U_n(\boldsymbol{x}_s) = \int_{\mathbb{R}^d} G_{ni}(\boldsymbol{x}_s - \boldsymbol{x}')F_i(\boldsymbol{x}')\,\mathrm{d}\boldsymbol{x}' + U_i(\boldsymbol{x}_s)I_{ni} \tag{A.2}$$

where

$$I_{ni} = \omega^2 \int_{\mathbb{R}^d} G_{ni}(\boldsymbol{x}_s - \boldsymbol{x}')\hat{\rho}(\boldsymbol{x}')\,\mathrm{d}\boldsymbol{x}'. \tag{A.3}$$

For a given forcing, Eq. (A.2) is a linear system of equations with the unknowns being the displacement components at the defect location, which takes the form

$$(\delta_{ni} - I_{ni})U_i(\boldsymbol{x}_x) = \int_{\mathbb{R}^d} G_{ni}(\boldsymbol{x}_s - \boldsymbol{x}')F_i(\boldsymbol{x}')\,\mathrm{d}\boldsymbol{x}'. \tag{A.4}$$

Upon solving this linear system for $\boldsymbol{U}(\boldsymbol{x}_s)$, one can proceed with the scattering analysis by inserting the solution into Eq. (A.1). When evaluating at a point $\boldsymbol{x}$ that is away from $\boldsymbol{x}_s$, the local perturbation approximation applies again to the final term in Eq. (A.1) allowing $G_{ni}(\boldsymbol{x} - \boldsymbol{x}_s)$ to be taken out of the integral, leading to

$$U_n(\boldsymbol{x}) = \int_{\mathbb{R}^d} G_{ni}(\boldsymbol{x} - \boldsymbol{x}')F_i(\boldsymbol{x}')\,\mathrm{d}\boldsymbol{x}' + \omega^2 U_i(\boldsymbol{x}_s)\hat{m}G_{ni}(\boldsymbol{x} - \boldsymbol{x}_s). \tag{A.5}$$

This is a generalized form of Eq. (33) for the three-dimensional case with arbitrary forcing, which is valid when evaluated away from $\boldsymbol{x}_s$.

## Appendix B. Evaluation of the 2D local perturbation integral

In this appendix, we evaluate the integral denoted $I$ that results from the local perturbation method, which is defined in Eq. (29). Evaluating $I$ involves integrating the perturbation density multiplied by the Green's function, which is necessary for computing scattered displacement field. We present a semi-analytical approach for the evaluation of $I$ in the two-dimensional case. In polar coordinates, the radial integral can be analytically evaluated, leaving a one-dimensional integral over the angular coordinate to be evaluated numerically.

First, we convert $I$ to polar coordinates $\boldsymbol{r} = (r, \theta)$ with the origin taken as point $\boldsymbol{x}_s$ within the defect. Converting $I$ of Eq. (29) to polar coordinates leads to

$$I = \omega^2 \int_0^{2\pi} \int_0^{\infty} G_{33}(\boldsymbol{r})\hat{\rho}(\boldsymbol{r}) r \,\mathrm{d}r \,\mathrm{d}\theta. \tag{B.1}$$

We consider a perturbation density of the form

$$\hat{\rho}(\boldsymbol{r}) = \begin{cases} \bar{\rho}, & r \leq R(\theta) \\ 0, & \text{else} \end{cases} \tag{B.2}$$

where $\bar{\rho}$ is a constant areal density inside the finite region enclosed by $R(\theta)$, which defines the shape of the defect. Thus, the overall mass of the perturbation is $\hat{m} = \bar{\rho}A$, where $A$ is the area enclosed by $R(\theta)$, corresponding to the area of the defect.

Before rewriting $G_{33}(\boldsymbol{x}' - \boldsymbol{x}_s)$ in polar coordinates, we first simplify notation by expressing the quantity $Z$ of Eq. (21) as

$$Z = (\boldsymbol{x}' - \boldsymbol{x}_s) \cdot \boldsymbol{w} \tag{B.3}$$

where $\boldsymbol{w}$ is defined as

$$w_i = \epsilon_{ji} \frac{\partial^2 \omega}{\partial k_j \partial k_l} \epsilon_{lm} V_m. \tag{B.4}$$

The two-dimensional Levi-Civita symbol is denoted $\boldsymbol{\epsilon}$, with components $\epsilon_{11} = \epsilon_{22} = 0$ and $\epsilon_{12} = -\epsilon_{21} = 1$. Rewriting the far-field lattice Green's function of Eq. (20) in polar coordinates and using the notation of Eq. (B.3), we obtain

$$G_{33}(\boldsymbol{r}) = \frac{\mathrm{i}|\Omega|\psi_{03}^* \psi_3 \exp\left[-\mathrm{i}\frac{\pi}{4}\mathrm{sgn}(w_1 \cos\theta + w_2 \sin\theta)\right] \exp\left[\mathrm{i}r(k_1 \cos\theta + k_2 \sin\theta)\right]}{2\omega\sqrt{2\pi r}\sqrt{|w_1 \cos\theta + w_2 \sin\theta|}} \tag{B.5}$$

where $\psi_{03}$ is the $\boldsymbol{e}_3$-component of the mode shape evaluated at the origin. The wave vector $\boldsymbol{k}$ corresponding to a stationary point, from Eq. (22), only varies with $\theta$ and is independent of the radial coordinate. Therefore, upon inserting Eq. (B.5) into (B.1), $I$ takes the form

$$I = \frac{\mathrm{i}\omega|\Omega|\psi_{03}^* \psi_{03} \hat{m}}{2A\sqrt{2\pi}} \int_0^{2\pi} \int_0^{R(\theta)} \sqrt{r} e^{\mathrm{i}r f_1(\theta)} f_2(\theta) \,\mathrm{d}r \,\mathrm{d}\theta. \tag{B.6}$$

To obtain Eq. (B.6), the mode shape is assumed to be constant over the defect area since the corresponding wavelength is assumed to be much larger than the defect. The functions $f_1(\theta)$ and $f_2(\theta)$ are defined as

$$f_1(\theta) = k_1 \cos\theta + k_2 \sin\theta \tag{B.7}$$

$$f_2(\theta) = \frac{\exp\left[-\mathrm{i}\frac{\pi}{4}\mathrm{sgn}(w_1\cos\theta + w_2\sin\theta)\right]}{\sqrt{|w_1\cos\theta + w_2\sin\theta|}}. \tag{B.8}$$

We denote the inner integral over $r$ in Eq. (B.6) as $I_r$, which is only dependent on $\theta$, such that

$$I = \frac{\mathrm{i}\omega|\Omega|\psi_{03}^{*}\psi_{03}\hat{m}}{2A\sqrt{2\pi}} \int_0^{2\pi} I_r(\theta)\,\mathrm{d}\theta. \tag{B.9}$$

Analytical evaluation of $I_r$ leads to

$$\begin{aligned} I_r = &\frac{f_2}{2} f_1{}^{-\frac{5}{2}} \Bigg( -2\mathrm{i}\sqrt{R}\cos\left(Rf_1\right) f_1{}^{\frac{3}{2}} + 2\sqrt{R}\sin\left(Rf_1\right) f_1{}^{\frac{3}{2}} + \mathrm{i}\mathcal{C}\left[\sqrt{\frac{2Rf_1}{\pi}}\right]\sqrt{2\pi} f_1 \\ &- \sqrt{2\pi}\mathcal{S}\left[\sqrt{\frac{2Rf_1}{\pi}}\right] f_1 \Bigg) \end{aligned} \tag{B.10}$$

where $\mathcal{C}[\cdot]$ and $\mathcal{S}[\cdot]$ are the Fresnel cosine integral function and the Fresnel sine integral function, respectively.

With $I_r$ written entirely of known quantities dependent only on $\theta$, what remains is to evaluate the one-dimensional integral of Eq. (B.9) over $\theta$. In the examples of the main text, we numerically integrate Eq. (B.9) using trapezoidal integration as the final step in evaluating $I$.

## Appendix C. Disorder example parameters

Table C.1: Randomly selected defect parameters for the example in Section 5.1.3.

| $x_1/a$ | $x_2/a$ | $\hat{m}/m$ |
|---|---|---|
| 9 | 3 | 1.9392 |
| 7 | 9 | 0.3166 |
| 12 | 9 | -0.6666 |
| 3 | 2 | -0.2258 |
| 3 | 10 | 0.2262 |
| 2 | 7 | 0.7847 |
| 12 | 10 | -0.2134 |
| 3 | 4 | 0.8085 |
| 11 | 2 | 1.1336 |
| 7 | 2 | -0.3348 |
| 12 | 5 | -0.6477 |
| 7 | 1 | -0.1100 |
| 10 | 11 | -0.0437 |
| 8 | 14 | 0.2725 |
| 13 | 10 | 0.5236 |
| 8 | 7 | -0.7435 |
| 9 | 7 | -0.2126 |
| 11 | 15 | 1.4030 |
| 3 | 5 | -0.9123 |
| 1 | 6 | 1.7866 |



## References


[1] R. N. Glaesener, S. Kumar, C. Lestringant, T. Butruille, C. M. Portela, and D. M. Kochmann, "Predicting the influence of geometric imperfections on the mechanical response of 2D and 3D periodic trusses," *Acta Materialia*, vol. 254, p. 118918, 2023.

[2] L. Brillouin, "Wave propagation in periodic structures," *McGraw-Hill*, vol. 2, pp. 2022–2025, 1946.

[3] I. Lifšic, "The scattering of short elastic waves in a crystal lattice, akad. nauk sssr," *Zhurnal Eksper. Teoret. Fiz*, vol. 18, pp. 293–300, 1948.

[4] M. Lifšic, "Some problems of the dynamic theory of non-ideal crystal lattices," *Il Nuovo Cimento (1955-1965)*, vol. 3, pp. 716–734, 1956.

[5] G. Koster, "Theory of scattering in solids," *Physical Review*, vol. 95, no. 6, p. 1436, 1954.

[6] E. W. Montroll and R. B. Potts, "Effect of defects on lattice vibrations," *Physical Review*, vol. 100, no. 2, p. 525, 1955.

[7] A. A. Maradudin, "Theory of lattice dynamics in the harmonic approximation," *Solid State Phys. Suppl.*, vol. 3, 1971.

[8] A. B. Movchan and L. I. Slepyan, "Band gap Green's functions and localized oscillations," *Proceedings of the Royal Society A: Mathematical, Physical and Engineering Sciences*, vol. 463, no. 2086, pp. 2709–2727, 2007.

[9] V. Zalipaev, A. Movchan, and I. Jones, "Waves in lattices with imperfect junctions and localized defect modes," *Proceedings of the Royal Society A: Mathematical, Physical and Engineering Sciences*, vol. 464, no. 2096, pp. 2037–2054, 2008.

[10] Z.-J. Yao, G.-L. Yu, Y.-S. Wang, and Z.-F. Shi, "Propagation of bending waves in phononic crystal thin plates with a point defect," *International Journal of Solids and Structures*, vol. 46, no. 13, pp. 2571–2576, 2009.

[11] A. A. Kutsenko, "Wave propagation through periodic lattice with defects," *Computational Mechanics*, vol. 54, pp. 1559–1568, 2014.

[12] M. Makwana and R. Craster, "Localised point defect states in asymptotic models of discrete lattices," *Quarterly Journal of Mechanics and Applied Mathematics*, vol. 66, no. 3, pp. 289–316, 2013.

[13] A. A. Kutsenko, "Explicit formula for amplitudes of waves in lattices with defects and sources and its application for defects detection," *European Journal of Mechanics-A/Solids*, vol. 54, pp. 209–217, 2015.

[14] B. Lal Sharma and G. Mishuris, "Scattering on a square lattice from a crack with a damage zone," *Proceedings of the Royal Society A*, vol. 476, no. 2235, p. 20190686, 2020.

[15] P. A. Martin, "Discrete scattering theory: Green's function for a square lattice," *Wave Motion*, vol. 43, no. 7, pp. 619–629, 2006.

[16] R. S. Langley, "The response of two-dimensional periodic structures to point harmonic forcing," *Journal of Sound and Vibration*, vol. 197, no. 4, pp. 447–469, 1996.

[17] P. A. Martin, *Multiple scattering: Interaction of time-harmonic waves with N obstacles*. No. 107, Cambridge University Press, 2006.

[18] F. Bass and M. Fix, "Influence of the shape of small scatterers upon their resonance features," *Physical Review E*, vol. 56, no. 6, p. 7235, 1997.

[19] W. B. Beydoun and A. Tarantola, "First Born and Rytov approximations: Modeling and inversion conditions in a canonical example," *The Journal of the Acoustical Society of America*, vol. 83, no. 3, pp. 1045–1055, 1988.

[20] M. Lázaro, R. Wiltshaw, R. V. Craster, and L. M. García-Raffi, "Analytical approximations for multiple scattering in one-dimensional waveguides with small inclusions," *Mechanical Systems and Signal Processing*, vol. 224, p. 112046, 2025.

[21] M. Martí-Sabaté and D. Torrent, "Edge modes for flexural waves in quasi-periodic linear arrays of scatterers," *APL Materials*, vol. 9, no. 8, 2021.

[22] X. Pu, A. Palermo, and A. Marzani, "A multiple scattering formulation for finite-size flexural metasurfaces," *Proceedings of the Royal Society A*, vol. 478, no. 2262, p. 20210669, 2022.

[23] M. Lázaro, M. Martí-Sabaté, R. V. Craster, and V. Romero-García, "Weak scattering formulation for flexural waves in thin elastic plates with point-like resonators," *arXiv preprint arXiv:2503.23351*, 2025.

[24] A. A. Mokhtari, Y. Lu, and A. Srivastava, "On the properties of phononic eigenvalue problems," *Journal of the Mechanics and Physics of Solids*, vol. 131, pp. 167–179, 2019.

[25] C. Dorn and D. M. Kochmann, "Ray theory for elastic wave propagation in graded metamaterials," *Journal of the Mechanics and Physics of Solids*, vol. 168, p. 105049, 2022.

[26] M. I. Hussein, M. J. Leamy, and M. Ruzzene, "Dynamics of phononic materials and structures: Historical origins, recent progress, and future outlook," *Applied Mechanics Reviews*, vol. 66, no. 4, p. 040802, 2014.

[27] C. Sugino, Y. Xia, S. Leadenham, M. Ruzzene, and A. Erturk, "A general theory for bandgap estimation in locally resonant metastructures," *Journal of Sound and Vibration*, vol. 406, pp. 104–123, 2017.

[28] A. Bensoussan, J.-L. Lions, and G. Papanicolaou, *Asymptotic analysis for periodic structures*, vol. 374. American Mathematical Soc., 1978.

[29] O. Oudghiri-Idrissi, B. B. Guzina, and S. Meng, "On the spectral asymptotics of waves in periodic media with Dirichlet or Neumann exclusions," *The Quarterly Journal of Mechanics and Applied Mathematics*, vol. 74, no. 2, pp. 173–221, 2021.

[30] A. M. Kosevich, *The crystal lattice: Phonons, solitons, dislocations, superlattices*. John Wiley & Sons, 2006.

[31] E. N. Economou, *Green's functions in quantum physics*, vol. 7. Springer Science & Business Media, 2006.

[32] K. Madine and D. Colquitt, "Dynamic Green's functions in discrete flexural systems," *The Quarterly Journal of Mechanics and Applied Mathematics*, vol. 74, no. 3, pp. 323–350, 2021.

[33] R. McPhedran, L. Botten, J. McOrist, A. Asatryan, C. M. de Sterke, and N. Nicorovici, "Density of states functions for photonic crystals," *Physical Review E*, vol. 69, no. 1, p. 016609, 2004.

[34] V. Cervenỳ, *Seismic ray theory*. Cambridge University Press, 2001.

[35] M. J. Lighthill, *Waves in fluids*. Cambridge University Press, 1978.

[36] M. J. Lighthill, "Studies on magneto-hydrodynamic waves and other anisotropic wave motions," *Philosophical Transactions of the Royal Society of London. Series A, Mathematical and Physical Sciences*, vol. 252, no. 1014, pp. 397–430, 1960.

[37] V. Buchwald, "Elastic waves in anisotropic media," *Proceedings of the Royal Society of London. Series A. Mathematical and Physical Sciences*, vol. 253, no. 1275, pp. 563–580, 1959.

[38] A. J. Zelhofer and D. M. Kochmann, "On acoustic wave beaming in two-dimensional structural lattices," *International Journal of Solids and Structures*, vol. 115, pp. 248–269, 2017.

[39] B. Telgen, V. Kannan, J.-C. Bail, C. Dorn, H. Niese, and D. M. Kochmann, "Rainbow trapping of out-of-plane mechanical waves in spatially variant beam lattices," *Journal of the Mechanics and Physics of Solids*, vol. 191, p. 105762, 2024.

[40] C. Dorn and D. M. Kochmann, "Conformally graded metamaterials for elastic wave guidance," *Extreme Mechanics Letters*, vol. 65, p. 102091, 2023.

[41] P. De Vries, D. V. Van Coevorden, and A. Lagendijk, "Point scatterers for classical waves," *Reviews of Modern Physics*, vol. 70, no. 2, p. 447, 1998.

[42] R. Wiltshaw, R. V. Craster, and M. P. Makwana, "Asymptotic approximations for bloch waves and topological mode steering in a planar array of neumann scatterers," *Wave Motion*, vol. 99, p. 102662, 2020.

[43] R. Wiltshaw, J. M. De Ponti, and R. V. Craster, "Analytical solutions for bloch waves in resonant phononic crystals: deep-subwavelength energy splitting and mode steering between topologically protected interfacial and edge states," *The Quarterly Journal of Mechanics and Applied Mathematics*, vol. 76, no. 2, pp. 163–209, 2023.

[44] F. Bass, V. Freilikher, and V. Prosentsov, "Electromagnetic wave scattering from small scatterers of arbitrary shape," *Journal of Electromagnetic Waves and Applications*, vol. 14, no. 3, pp. 269–283, 2000.

[45] F. G. Bass and L. Vatova, "Investigation of eigen frequencies of a medium with local perturbations and spectrum of photon crystals," *Journal of Nanophotonics*, vol. 4, no. 1, p. 043507, 2010.

[46] M. Born and E. Wolf, *Principles of optics: electromagnetic theory of propagation, interference and diffraction of light*. Elsevier, 2013.

[47] A. S. Phani, J. Woodhouse, and N. Fleck, "Wave propagation in two-dimensional periodic lattices," *The Journal of the Acoustical Society of America*, vol. 119, no. 4, pp. 1995–2005, 2006.

[48] Mechanics and Materials Lab, "ae108," 2020. https://doi.org/10.5905/ethz-1007-257.

[49] S. G. Johnson, "The NLopt nonlinear-optimization package." https://github.com/stevengj/nlopt, 2007.

[50] D. C. Liu and J. Nocedal, "On the limited memory BFGS method for large scale optimization," *Mathematical Programming*, vol. 45, no. 1, pp. 503–528, 1989.

[51] J. R. Tempelman, T. Weidemann, E. B. Flynn, K. H. Matlack, and A. F. Vakakis, "Physics-informed machine learning for the inverse design of wave scattering clusters," *Wave Motion*, vol. 130, p. 103371, 2024.

[52] J. R. Capers, "Inverse design of thin-plate elastic wave devices," *Physical Review Applied*, vol. 20, no. 3, p. 034064, 2023.

**Declaration of interests**

The authors declare that they have no known competing financial interests or personal relationships that could have appeared to influence the work reported in this paper.